This is to certify that the
dissertation entitled

INVESTIGATION OF NONLINEAR OPTICAL CHROMOPHORE SURFACE DISTRIBUTION VIA SECOND HARMONIC MICROSCOPY

presented by

Michelle Christine Rini

has been accepted towards fulfillment
of the requirements for the

Doctoral degree in Chemistry

Major Professor's Signature

5/10/05

Date

INVESTIGATION OF NONLINEAR OPTICAL CHROMOPHORE SURFACE DISTRIBUTION VIA SECOND HARMONIC MICROSCOPY

By

Michelle Christine Rini

A DISSERTATION

Submitted to
Michigan State University
in partial fulfillment of the requirements
for the degree of

DOCTOR OF PHILOSOPHY

Department of Chemistry

2005

ABSTRACT

INVESTIGATION OF NONLINEAR OPTICAL CHROMOPHORE SURFACE DISTRIBUTION VIA SECOND HARMONIC MICROSCOPY

By

Michelle Christine Rini

We have constructed a surface second harmonic imaging system capable of acquiring spatially-resolved surface second harmonic data with diffraction-limited resolution. For a 100x magnification microscope objective of numerical aperture 0.55, we achieve a resolution of ~0.5μm. We have used surface second harmonic imaging measurements to characterize the heterogeneous structure of organic compounds bound to silica substrates using zirconium bisphosphonate chemistry. Previous second harmonic generation intensity measurements of these surfaces have revealed multiple domains, but it was not possible to elucidate the characteristic domain sizes.

The images acquired for a series of silica surfaces modified with controlled amounts of a rigid $\chi^{(2)}$ chromophore reveal the presence of two domains, with characteristic sizes of ~1 μm and ~ 15 μm, and with the relative contribution of each domain changing with the composition of the imaged monolayer. To extract this information from the experimental surface second harmonic images, we have applied a correlation-based analysis and provide a detailed description of this methodology in Chapter 2. The presence of multiple domains underscores the heterogeneous nature of

silica surfaces and the need for spatially resolved information to characterize the heterogeneity

We have also fabricated two multilayer assemblies of the nonlinear chromophores (4-(4-(4-(4-((2-Hydroxyethyl) sulfonyl) phenyl) piperazinyl)-phenyl) phosphonic acid **(C1)** and (2-(4-(4-(4-(4-hydroxyphenyl)piperazinyl)phenyl)azophenyl)sulfonyl) ethylphosphonic acid **(C2)**. The C1 multilayer assembly exhibits a decreasing degree of correlation as the number of deposited layers increases. In the context of island like deposition of ZP films this result is reasonable since small islands are less likely to be correlated and begin to resemble a randomized surface. Average feature sizes calculated for the C1 sample were ~11μm, in reasonable agreement with the larger feature size observed in the monolayer experiments of chapter three (~15μm). The C2 multilayer assembly produced feature sizes of ~10μm, also in fair agreement with the monolayer results. In contrast with the C1 assembly, however, no decrease in correlation was observed with increasing number of layers. The absence of a similar trend to the C1 sample was unexpected considering the similarity in structure between C1 and C2.

To My Mother

ACKNOWLEDGMENTS

First, I would like to express my gratitude to my advisor Dr. Gary Blanchard. Your advice and insight have always been appreciated and whatever success I have enjoyed here would not have been possible without your support. To the members of the Blanchard group, both past and present...WOW! I've met some interesting characters here and I'll never forget any of you.

My especial thanks to Dr. Jaycoda S. Major, you are one of the best friends I've made in graduate school. We went through our wild and crazy phases together and I miss you being around. From the old crew: Lee, you are the best story teller I've ever met and to me 'dog' will always mean 'pig!'; DJ Tulock, thanks for the many rock out nights in the lab; and of course Steve, I am never going to Eisenthal! But seriously Steve, you give the best pep talks in the whole world and you'll be a great daddy. From the new crew: Alex...what can I say dude? Without game night I'd be dead in a ditch somewhere. When I finally leave Lansing I'll miss our get togethers. To my best friend Amy, thank you for listening to me pontificate about everything under the sun and never telling me to shut up. Last but certainly not least, Matt. Your love and support have been unflagging and I can't express my gratitude enough.

Finally, to my family, especially my parents: THANK YOU! Without all of your love, support, and prayers I would not have made it through this endeavor at all. You are first and foremost in my heart and I love you all.

If you don't find your name in these acknowledgements it isn't because you're not remembered, there are just too many names to fit. So thank you everyone and goodbye!

TABLE OF CONTENTS

LIST OF TABLES

LIST OF FIGURES

LIST OF ABBREVIATIONS

AC ..... autocorrelation function

C1 ..... (4-(4-(4-(4-((2-hydroxyethyl) sulfonyl)phenyl)piperazinyl)-phenyl) phosphonic Acid

C2 ..... (2-(4-(4-(4-(4-hydroxyphenyl)piperazinyl)phenyl)azophenyl)sulfonyl) ethylphosphonic Acid (C2)

CCD ..... charge couple device

DO3 ..... disperse orange 3

DR ..... dynamic range

DR1 ..... disperse red 1

HDPA ..... 1-hydroxyl-12-dodecylphosphonic acid

KD*P ..... potassium dideuterium phosphate

LB ..... Langmuir-Blodgett

LN_2 ..... liquid nitrogen

NA ..... numerical aperture

Nd:YAG ..... neodymium:yttrium aluminum garnet

NLO ..... nonlinear optical

PEM ..... polyelectrolyte multilayers

PMT ..... photomultiplier tube

SAM ..... self assembled monolayer(s)

SHG ..... second harmonic generation

SHM ..... second harmonic microscopy

SNR ..... signal to noise ratio

TIR ..... total internal reflection

UHV ..... ultra high vacuum

ZP ..... zirconium phosphate/phosphonate

Chapter 1

INTRODUCTION

The ability to tailor the properties of surfaces and interfaces is of great importance for applications in areas such as chemical and biological sensing,[1-4] insulating and passivating coatings,[5-8] wetting and adhesion,[9-12] and molecular electronics.[13-15] Molecular control over surface modification can be achieved through use of self-assembled mono- and multilayer (SAM) thin films including Langmuir-Blodgett (LB) films,[16] alkanethiols on coinage metals,[17, 18] polyelectrolytes,[19, 20] and zirconium phosphate/phosphonate (ZP) type films.[21, 22] As the breadth and scope of surface modification research increases, so do the methods by which these surfaces are characterized.

Second harmonic generation (SHG) has long been a useful and powerful tool in the investigation of surfaces and interfaces, combining the surface selectivity of particle scattering techniques with the advantages of optical spectroscopy. Within the last decade the utility of SHG has been extended further through the technique of second harmonic microscopy. While obtaining a surface second harmonic micrograph is an important step in the development of this technique, a method to further analyze and extract information from these micrographs is also desirable. *The focus of this work is to utilize second harmonic microscopy to image modified surfaces and to develop an analysis protocol to interpret the resulting images.*

As mentioned above, molecular control over surface modification can be achieved through chemical systems capable of self-assembly. In Langmuir-Blodgett type films,

physisorption is the mechanism by which adlayers interact with the substrate and with each other. Since LB films are held together through relatively weak van der Waals attractions, they are easily perturbed. While LB films offer orientational control over adsorption and possess substantial lateral freedom, they are not robust in nature.

Alkanethiols adsorbed on gold surfaces provide an improvement over LB films in terms of substrate-adsorbate interactions. In alkanethiols, the sulfur head group is chemisorbed onto the gold substrate as opposed to the physisorbed nature of LB films. Alkanethiols are perhaps the most well characterized SAM systems. Under solution phase deposition conditions, they are known to achieve surface coverages approaching that of a closest packed monolayer. Such high surface coverages (typically ~90% of a closest packed monolayer) are attributed to high mobility of the adsorbate species.[23] Tarlov and Newman have also shown that alkanethiol films, oxidized under ambient laboratory conditions, exhibit displacement of the sulfonate species by thiol upon re-immersion of the film in thiol solution.[24] The replacement of oxidized species indicates a dynamic equilibrium between solution phase thiols and those adsorbed to the surface.

Long chain alkanethiols are also popular choices for passivation layers since films that are largely free of defects exhibit resistance to ion penetration and electron transfer. Surface priming is another useful application of functionalized alkanethiol SAMs. Since the sulfur headgroup is preferentially adsorbed on gold, a variety of terminal functionalities may be presented to the ambient interface and used for further reactive chemistry.[25, 26] However, despite all of the highlighted benefits of alkanethiols, including highly ordered monolayer structures and facile preparation; there are some significant

drawbacks to using them. Alkanethiols are not amenable to building regular multilayer structures and they also require a metal substrate for layer growth.

Polyelectrolyte multilayer (PEM) films use electrostatic interactions to achieve layer growth. PEM films have been used widely as components in composite membranes for separations and filtration.[27-30] Deposition conditions for polyelectrolyte adsorption are mild and are usually performed in aqueous solution. The wide variety of polyanions and polycations available make polyelectrolyte films quite versatile and they can be uniquely tailored to the specific requirements of the application. Although layer-by-layer deposition of polyelectrolytes is possible and layer *thickness* may be controlled in this manner, the adlayer constituents are polymeric in nature so there is no control over the orientation or direction of adsorption. Another disadvantage of polyelectrolytes is the degree of interpenetration between adlayers,[31, 32] making discreet layers difficult to differentiate.

Many chemical systems capable of self-assembly use the formation of covalent bonds between the adlayer and the substrate to effect layer growth. Examples of some covalent interlayer linking chemistries include the formation of amide, ester, urea, and urethane bonds.[33, 34] The stability of the covalent bond offers superior resistance to thermal damage and to degradation by solvent than either LB films or alkanethiols, which are particularly susceptible to desorption. Also, dielectric materials may be investigated since their surfaces can easily be primed to produce a terminal functionality conducive to layer growth through covalent attachment.

Like alkanethiols, ZP films belong to the class of SAM systems that interact with the substrate via covalent bonding. Pioneered by both Mallouk[21, 35-39] and

Thompson[22, 40, 41] in the early 1990's, zirconium organophosphate films have been widely used to assemble robust mono- and multilayered structures. In general, the metal-phosphonate salts form insoluble complexes that often resemble their inorganic metal-phosphate analogs. Zirconium organophosphates form puckered sheets from the metal ions and the phosphonate oxygens, with the zirconium ions in the same plane (see Figure 1.1).[38]

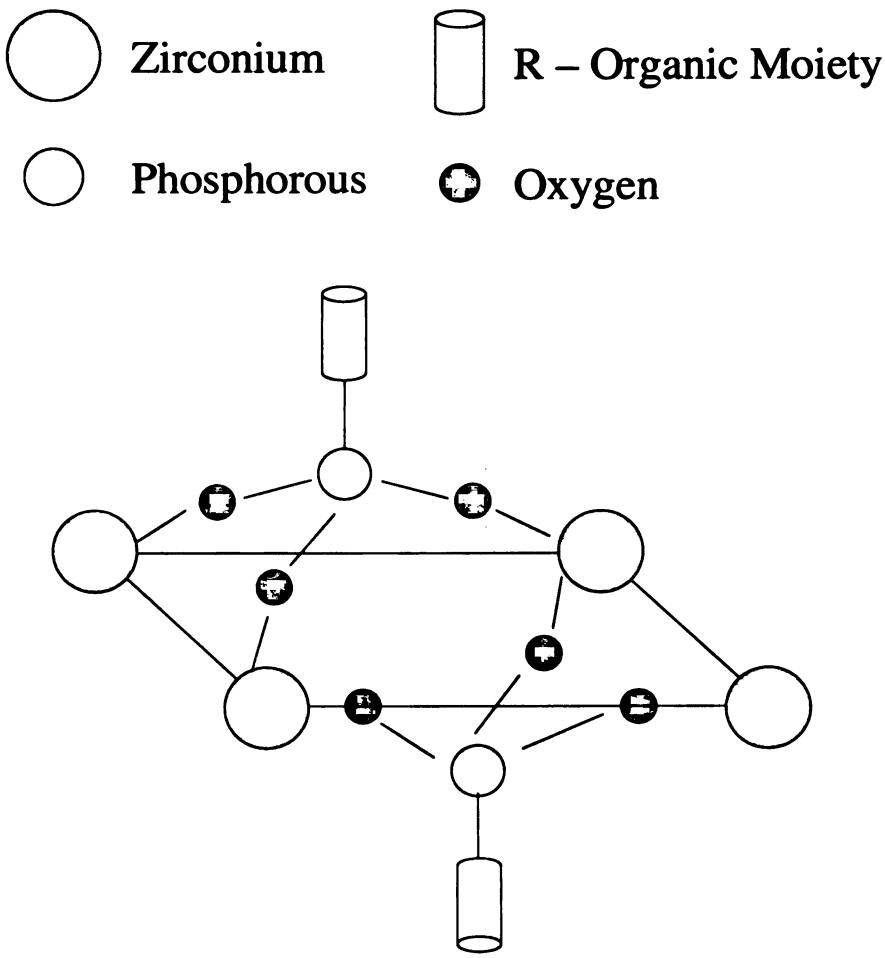

Figure 1.1: Illustration of zirconium organophosphate puckered sheet formation. Zirconium ions lie in the same plane with phosphonate groups lying above and below.

As long as the phosphonate group is present for layer growth, the body of the organic moiety can be as diverse as the application demands or the imagination dictates. Of primary interest in this work is the application of ZP film growth to developing nonlinear optical materials. Katz and co-workers developed an efficient strategy for producing layered assemblies of nonlinear optical chromophores using ZP interlayer linking chemistry.[42] We adopt the use of their chromophore 1 in this work (denoted C1 here) due not only to the control of adsorption orientation but also to its substantial second order nonlinear susceptibility ($\beta = 150 \times 10^{-30}$ esu at 1064nm).

The second harmonic response of a material depends on the concentration (or surface density) of molecules at the interface, the components of the $\chi^{(2)}$ tensor (which relates the polarization response of the bulk material to the electric field), the intensity of the electric field, and the molecular orientational distribution. Second harmonic generation is a nonlinear spectroscopic technique that combines the surface selectivity of particle scattering methods with the advantages of optical spectroscopy. Although particle scattering techniques are surface selective, they must be carried out under ultra high vacuum (UHV) conditions. The restriction to UHV also limits the types of surfaces accessible to investigation, effectively eliminating the liquid phase as an interfacial component. More traditional optical spectroscopic methods involving absorption, emission, and Raman scattering often lack the ability to differentiate signal contributions from bulk and interfacial species. SHG is a second order, nonlinear optical process which combines two photons at fundamental frequency ω to produce a single photon at frequency 2ω. SHG is also inherently surface-selective due to symmetry constraints such that, within the dipole approximation, only non-centrosymmetric environments produce

second harmonic signal. At an interface this condition is necessarily met since the bulk phases differ from one another. Second harmonic generation also retains the high sensitivity of more traditional optical spectroscopic methods; typically sensing sub-monolayer adsorbate concentrations and having good spatial, temporal, and spectral resolution. SHG is non-destructive to the sample and in principle, can be used *in situ* to study any interface accessible to light without interference from the bulk.

For example, by measuring second harmonic intensity with varying combinations of input and output polarization, an assessment of molecular order and orientation is possible. The Richmond group has used such a technique to study the interfacial region for several alkane/water interfaces using SHG in total internal reflection (TIR) geometry.[43] The TIR geometry provides an enhancement of the non-resonant SH signal so that the neat interface can be investigated without a probe molecule. It is worth noting that the liquid/liquid interface is not amenable to investigation by any particle scattering technique since liquids are inappropriate for UHV studies and do not provide a long enough mean free path for the particle. The TIR enhancement of the SH signal arises from the generation of an evanescent wave along the interface and the increased propagation length of the fundamental field. By increasing the propagation length of the fundamental field the phase matching of the evanescent wave also increases, producing an enhancement of the second harmonic signal.

Four n-alkane/water interfaces were studied by Richmond's group, from heptane to decane and the degree of order at these interfaces was evaluated by a ratio of $\chi^{(2)}_{izi}$ ($i = x,y$) tensor elements. It was found that the even numbered alkane systems exhibited a higher degree of order than the odd numbered alkane/water interfaces. This difference

in the degree of order at the interface was attributed to a possible difference in the packing arrangement of even and odd-numbered alkanes in the condensed phase.

There is a large body of literature on second harmonic generation as a tool for probing interfacial systems and several reviews of the field have been published.[44-46] Interfacial information concerning adsorption, molecular orientation, surface symmetry, and reaction kinetics is accessible through second harmonic experiments. Not only are liquid/liquid[43, 47-56] interfaces accessible, like the experiment of Richmond described earlier, but liquid/solid,[55, 57-61] air/liquid,[62-64] and air/solid[42, 65-74] interfacial systems have also been studied via SHG.

For example, the interfacial adsorption and the orientation of organic molecules have been investigated for many of the interfaces listed above. At the water / 1,2 - dichloroethane (DCE) interface, Corn's group has studied the co-adsorption of a charged biopolymer, poly-L-glutamic acid (pGlu), and two surfactants containing a $\chi^{(2)}$-active, hemicyanine chromophore.[75] The co-adsorption mechanism was proposed to be a multipoint, electrostatic interaction between the poly-L-glutamic acid and the cationic surfactant. The two surfactants used in the study were the cationic species *trans*-4-[4-(dibutylamino)styryl]-1-methylpyridinium iodide (D+-CH_3) and the neutral species *trans*-4-[4-(dibutylamino)styryl]-1-(3-sulfopropyl)pyridinium hydroxide inner salt hydrate (D+-$(CH_2)_3$-SO_{3^-}). Surface coverage of each of the adsorbed surfactant molecules at the water-DCE interface (in the absence of biopolymer) was first monitored via resonant SHG. The interfacial, molecular orientation of both surfactants was determined to be ~43° and did not change during the course of the experiments involving biopolymer, indicating that the second harmonic intensity was directly related to surface coverage.

For experiments involving poly-L-glutamic acid, the SH intensity was monitored in time after pGlu was injected. An increase in SH intensity was observed upon injection of pGlu to the cationic species D+-CH_3 but not for the neutral surfactant D+-$(CH_2)_3$-SO_3-, confirming the electrostatic nature of the co-adsorption process. When the cationic surfactant system was injected with the monomer L-glutamic acid, no increase in second harmonic intensity was observed indicating that the interaction between pGlu and D+-CH_3 occurs over multiple points of the polymer.

Shen's group has studied the orientation of cavitand molecules at the air/fused silica interface.[70] In this study SHG was used as a qualitative measure of molecular orientation as opposed to the absolute measure of molecular tilt angle. Cavitands are rigid, bowl-shaped molecules that can act as synthetic receptors by participating in guest-host type interactions. The cavitands studied by Shen's group were comprised of hydrophilic, vase-like heads and long, aliphatic tails. When the cavitand molecules were adsorbed onto bare silica it was found that the head groups were oriented towards the silica surface. If the silica surface was first modified with a long-chain surfactant, then the aliphatic tails of the cavitand molecules could be made to orient themselves towards the surface and the head groups were then exposed for possible use in sensing applications.

Also at the air/fused silica interface, the order and orientation of malachite green was investigated by Leach and co-workers.[76] The average molecular tilt angle, with respect to the surface normal, obtained for malachite green was $8.2° \pm 0.5°$. Such a low tilt angle indicates that malachite green forms adlayers in which the molecule is upright and approximately parallel to the surface. The authors attribute this conformational

arrangement to the interaction of the dimethyl-amino substituents of malachite green with the substrate.

At the glass-water interface, Eisenthal's group has investigated the adsorption and orientation of an oxazole dye on a supported lipid bilayer.[77] Phospholipid bilayers are popular model systems for the study biomembranes. In this experiment, the bilayer was formed from a mixture of the phospholipids 1, 2-Dioleoyl-sn-Glycero-3-phosphocholine (DOPC) and 1,2-Dioleoyl-sn-Glycero-3-[Phospho-rac-(1-glycerol)] (DOPG). The negatively charged lipid bilayer was grown on the underside of a Dove prism and the resonant second harmonic signal from the surface was monitored in time. Upon injection of the SH-active dye molecule 4-[5-metho-xyphenyl)-2-oxazolyl]pyridinium methanesulfonate (4PyMPO-MeMs) a large increase in second harmonic intensity was observed. Since the oxazole dye was positively charged at neutral pH it was expected to adsorb strongly to the negatively charged lipid bilayer. The observed increase in intensity remained constant over the course of the experiment, ~4hours, and the tilt angle of adsorbed dye was determined to be $19^{\circ} \pm 2^{\circ}$.

In the context of molecular orientation, it is worthwhile to note the work done by Simpson and Rowlen on the effect of the distribution width of the molecular tilt angles on the apparent tilt angle.[78] When determining the mean molecular tilt angle from second harmonic experiments, a frequent assumption is that the distribution of tilt angles around the mean is narrow and can be approximated by a δ-function. For systems other than a close-packed monolayer, however, the δ-function approximation may be a poor one. Calculations were performed varying the distribution width, $0^{\circ} \leq \sigma \leq 70^{\circ}$, and the mean distribution tilt angle, $0^{\circ} \leq \theta_o \leq 89^{\circ}$, to observe the effect on the apparent tilt angle (the tilt

angle obtained by assuming a δ-function distribution). Two important results were obtained from these calculations: 1.) for broad distribution widths, the apparent molecular tilt angle deviates significantly from the true distribution mean, and 2.) each curve converges to an apparent molecular tilt angle of 39.2°, the so-called 'magic angle' for SHG.

This brief discussion on the use of SHG to elucidate information on interfacial molecular orientation shows the utility of such a surface selective technique at many types of condensed phase interfaces. Although determining molecular orientation at the interface is not the only application of SHG it is a ubiquitous one. Advancements in the development of $\chi^{(2)}$ - active organic chromophores[79-82] also continue to open new pathways to the use of SHG as a surface probe. Species which are not normally SH-active, such as proteins, can be 'tagged' with $\chi^{(2)}$-active chromophores in order to monitor their behavior at interfaces.[83] Another venue where second harmonic generation has been usefully applied is in the field of microscopy. Second harmonic microscopy can provide information on the surface distribution of $\chi^{(2)}$-active chromophores that the intensity experiment cannot.

Second harmonic microscopy was first reported by Gannaway and Sheppard in 1978. In that work the second harmonic light generated from nonlinear optical (NLO) crystals of potassium dideuterium phosphate (KD*P) and $LiNbO_3$ were imaged using a raster scanning technique. The second harmonic micrographs obtained showed fine structure in the crystal not resolvable under a conventional microscope.[84] Since then SH microscopy has slowly developed as a surface imaging technique. It retains all the

benefits of second harmonic generation as an interfacial probe, while providing information about the *distribution* of NLO active species.

Second harmonic microscopy (SHM) has been used to study surface diffusion,[85-89] thin films,[90-94] biological systems,[92, 93, 95, 96] and the NLO response of nanowires.[97] Schultz and Seebauer employed second harmonic microscopy to study the surface diffusion of Sb on a Ge(111) surface at greater than 50% of the substrate melting temperature. SHM avoids the surface damage and inadvertent chemistry induced by most ion or electron probes and is operable under a range of temperatures and pressures. Also, because second harmonic microscopy is an optical probe, it has high enough sensitivity to measure sub-monolayer adsorbate concentrations and the short diffusion lengths of those adsorbates. Finally, unlike ion and electron probes the spatially resolved second harmonic intensity may be expressed as a function of surface coverage. Therefore, the diffusivity as a function of surface coverage is accessible. In the experiments of Schultz and Seebauer, diffusivities of Sb as a function of surface coverage, θ, were extracted from step profiles of SH intensity vs. pixel position. It was found that the diffusivity decreased greatly as the surface coverage of Sb increased. It was also found that in the coverage range examined, the calculated activation energy and pre-exponential factor were more consistent with an adatom vacancy model than with a site-to-site hopping model.[89]

Turning away from surface diffusion measurements, SHM has also been used by Flörsheimer et al. to investigate the distribution of ferroelectric domains at the air/water interface.[98] They were interested in laterally resolving the local features of a Langmuir-Blodgett film and observing the changes in the distribution of molecular orientations

directly. Such an investigation was not possible with a conventional second harmonic generation experiment since conventional SHG probes interfacial orientation averaged over the illuminated spot size.

Flörsheimer's group made an improvement to the experiment of Schultz and Seebauer by replacing the photodiode array with a charge couple device (CCD) camera. This enabled the SH signal to be detected in parallel, precluding the need to scan or raster the sample, and as a result SH micrographs of the LB film at the interface were obtained. The contrast observed in the images was attributed to the orientational variation of local structural features, assuming that all local features possessed the same susceptibility tensor.

Non-centrosymmetry in the surface plane was probed using a collinear beam geometry with normal incidence to the sample. To probe dipoles normal to the surface plane, an oblique angle of incidence was required and a crossed-beam geometry was adopted. Not only did the crossed-beam geometry provide access to dipoles normal to the surface plane, it also permitted a diffraction limited image to be acquired over the entire object field instead of just a small strip. Flörsheimer et al. also proposed that second harmonic microcopy could be extended to near-field imaging to improve the lateral resolution of the technique.

Saykally and co-workers have used second harmonic near field optical microscopy quite effectively in order to image granular membranes in natural killer cells and zinc oxide nanowires, achieving sub-diffraction limit resolution.[92, 97]

While acquiring a second harmonic micrograph is important in and of itself, it is a non-trivial task to extract additional information from it. In this work we were interested

in not only the imaging of amorphous surfaces, such as quartz, but also in developing an analysis protocol able to extract characteristic domain size information from the image. We chose an autocorrelation approach in developing the analysis procedure and while this is not a new technique,[99-102] it has not been widely applied to the analysis of second harmonic micrographs.

Chapter 2 of this document provides a brief theoretical discussion of the origins of second harmonic generation, the mathematical nature of the autocorrelation function, and the instrumental design of the second harmonic microscope. Relevant instrumental parameters such as signal-to-noise ratio, depth of field, and dynamic range are also treated in Chapter 2 along with the conditions for image acquisition and analysis. The contents of Chapter 2 concerning data acquisition outline general procedures for image acquisition and data processing followed for all systems studied. Specific experimental procedures appear in the appropriate data chapter.

Experiments performed by varying the composition of a chromophore containing monolayer are detailed in Chapter 3 and Chapter 4 concerns the study of multilayer assemblies. Chapter 5 summarizes the conclusions of this work and gives several avenues of future investigation.

1.1 Literature Cited

1. Cao, G. and Mallouk, T.E.; *Inorg. Chem.*, **1991**, *30*(7), 1434.

2. Frink, K.J., Wang, R.C., Colon, J.L., and Clearfield, A.; *Inorg. Chem.*, **1991**, *30*(7), 1438.

3. Snejdarkova, M., Rehak, M., and Otto, M.; *Anal. Chem.*, **1993**, *65*(6), 665.

4. Hianik, T., Snejdarkova, M., Passechnik, V.I., Rehak, M., and Babincova, M.; *Bioelectrochem. Bioenerg.*, **1996**, *41*(2), 221.

5. Katz, H.E. and Schilling, M.L.; *Chem. Mater.*, **1993**, *5*(8), 1162.

6. Schilling, M.L., Katz, H.E., Stein, S.M., Shane, S.F., Wilson, W.L., Ungashe, S.B., Taylor, G.N., Putvinski, T.M., Chidsey, C.E.D., and Buratto, S.; *Langmuir*, **1993**, *9*(8), 2156.

7. Harder, P.G., M.; Dahint, R.; Whitesides, G.M.; Laibinis, P.E.; *Journal of Physical Chemistry B*, **1998**, *102*(426.

8. Prime, K.L.W., G.M.; *Science*, **1991**, *252*(1164.

9. Dubois, L.H., Zegarski, B.R., and Nuzzo, R.G.; *J. Am. Chem. Soc.*, **1990**, *112*(2), 570.

10. Bain, C.D.W., G.M.; *Journal of the Ameican Chemical Society*, **1988**, *110*(5897.

11. Bain, C.D. and Whitesides, G.M.; *J. Am. Chem. Soc.*, **1988**, *110*(11), 3665.

12. Stewart, K.R.W., G.M.; Godfried, H.P.; Silvera, I.F.; *Rev. Sci. Instrum.*, **1986**, *57*(1381.

13. Tour, J.M.; *Accounts of Chemical Research*, **2000**, *33*(791.

14. Joachim, C.G., J. K.; Aviram, A.; *Nature*, **2000**, *408*(541.

15. Hanggi, P.R., M.; Yaliraki, S.; *Chem. Phys.*, **2002**, *281*(111.

16. Langmuir, I.; *J. Am. Chem. Soc.*, **1917**, *39*(1848.

17. Ulman, A. and Editor, Self-Assembled Monolayers of Thiols. [In: Thin Films (San Diego), 1998; 24]. 1998.

18. Rieley, H., Kendall, G.K., Jones, R.G., and Woodruff, D.P.; *Langmuir*, **1999**, *15*(26), 8856.

19. Decher, G.H., J. D.; Schmitt, J.; *Thin Solid Films*, **1992**, *210/211*(831.

20. Krasemann, L. and Tieke, B.; *Materials Science & Engineering, C: Biomimetic and Supramolecular Systems*, **1999**, *C8-C9*(513.

21. Lee, H., Kepley, L.J., Hong, H.G., Akhter, S., and Mallouk, T.E.; *J. Phys. Chem.*, **1988**, *92*(9), 2597.

22. Vermeulen, L.A., Snover, J.L., Sapochak, L.S., and Thompson, M.E.; *J. Am. Chem. Soc.*, **1993**, *115*(25), 11767.

23. Nuzzo, R.G., Fusco, F.A., and Allara, D.L.; *J. Am. Chem. Soc.*, **1987**, *109*(8), 2358.

24. Tarlov, M.J. and Newman, J.G.; *Langmuir*, **1992**, *8*(5), 1398.

25. Lahann, J., Mitragotri, S., Tran, T.-N., Kaido, H., Sundaram, J., Choi Insung, S., Hoffer, S., Somorjai Gabor, A., and Langer, R.; *Science*, **2003**, *299*(5605), 371.

26. Sigal, G.B., Bamdad, C., Barberis, A., Strominger, J., and Whitesides, G.M.; *Anal. Chem.*, **1996**, *68*(3), 490.

27. Miller, M.D. and Bruening, M.L.; *Langmuir*, **2004**, *20*(26), 11545.

28. Miller, M.D., Baker, G.L., and Bruening, M.L.; *J. Chromatogr., A*, **2004**, *1044*(1-2), 323.

29. Kang, S.H.C., Y. K.; Chang, H. N.; *Biotechnol. Prog.*, **2004**, *20*(3), 764.

30. Pontie, M., Diawara, C., Rumeau, M., Aureau, D., and Hemmery, P.; *Desalination*, **2003**, *158*(1-3), 277.

31. Laurent, D. and Schlenoff, J.B.; *Langmuir*, **1997**, *13*(6), 1552.

32. Baur, J.W., Rubner, M.F., Reynolds, J.R., and Kim, S.; *Langmuir*, **1999**, *15*(19), 6460.

33. Major, J.S. and Blanchard, G.J.; *Chem. Mater.*, **2002**, *14*(6), 2574.

34. Major, J.S. and Blanchard, G.J.; *Chem. Mater.*, **2002**, *14*(6), 2567.

35. Hong, H.G., Sackett, D.D., and Mallouk, T.E.; *Chem. Mater.*, **1991**, *3*(3), 521.

36. Kaschak, D.M., Johnson, S.A., Hooks, D.E., Kim, H.-N., Ward, M.D., and Mallouk, T.E.; *J. Am. Chem. Soc.*, **1998**, *120*(42), 10887.

37. Fang, M., Kaschak, D.M., Sutorik, A.C., and Mallouk, T.E.; *J. Am. Chem. Soc.*, **1997**, *119*(50), 12184.

38. Cao, G., Hong, H.G., and Mallouk, T.E.; *Acct. Chem. Res.*, **1992**, *25*(9), 420.

39. Kerimo, J., Adams, D.M., Barbara, P.F., Kaschak, D.M., and Mallouk, T.E.; *J. Phys. Chem. B*, **1998**, *102*(47), 9451.

40. Byrd, H., Snover, J.L., and Thompson, M.E.; *Langmuir*, **1995**, *11*(11), 4449.

41. Snover, J.L. and Thompson, M.E.; *J. Am. Chem. Soc.*, **1994**, *116*(2), 765.

42. Katz, H.E., Wilson, W.L., and Scheller, G.; *J. Am. Chem. Soc.*, **1994**, *116*(15), 6636.

43. Conboy, J.C., Daschbach, J.L., and Richmond, G.L.; *J. Phys. Chem.*, **1994**, 9688.

44. Corn, R.M. and Higgins, D.A.; *Chem. Rev.*, **1994**, *94*(1), 107.

45. Eisenthal, K.B.; *J. Phys. Chem.*, **1996**, *100*(31), 12997.

46. Shen, Y.R.; *Nature (London, United Kingdom)*, **1989**, *337*(6207), 519.

47. Conboy, J.C. and Richmond, G.L.; *Electrochim. Acta*, **1995**, *40*(18), 2881.

48. Conboy, J.C. and Richmond, G.L.; *J. Phys. Chem. B*, **1997**, *101*(6), 983.

49. Fujiwara, K., Monjushiro, H., and Watarai, H.; *Chem. Phys. Lett.*, **2004**, *394*(4-6), 349.

50. Grubb, S.G., Kim, M.W., Rasing, T., and Shen, Y.R.; *Langmuir*, **1988**, *4*(2), 452.

51. Higgins, D.A., Naujok, R.R., and Corn, R.M.; *Chem. Phys. Lett.*, **1993**, *213*(5-6), 485.

52. Kott, K.L., Higgins, D.A., McMahon, R.J., and Corn, R.M.; *J. Am. Chem. Soc.*, **1993**, *115*(12), 5342.

53. Paul, H.J. and Corn, R.M.; *J. Phys. Chem. B*, **1997**, *101*(23), 4494.

54. Perrenoud-Rinuy, J., Brevet, P.-F., and Girault, H.H.; *Physical Chemistry Chemical Physics*, **2002**, *4*(19), 4774.

55. Uchida, T., Yamaguchi, A., Ina, T., and Teramae, N.; *J. Phys. Chem. B*, **2000**, *104*(51), 12091.

56. Nochi, K.Y., A.; Hayashita, T.; Uchida, T.; Teramae, N.; *J. Phys. Chem. B*, **2002**, *106*(38), 9906.

57. Burke, B.J., Moad, A.J., Polizzi, M.A., and Simpson, G.J.; *J. Am. Chem. Soc.*, **2003**, *125*(30), 9111.

58. Daschbach, J.L., Fischer, P.R., Gragson, D.E., and Richmond, G.L.; *J. Phys. Chem.*, **1995**, *99*(10), 3240.

59. Mifflin, A.L., Gerth, K.A., Weiss, B.M., and Geiger, F.M.; *J. Phys. Chem. A*, **2003**, *107*(32), 6212.

60. Shang, X.L., Y.; Yan, E.; Eisenthal, K. B.; *J. Phys. Chem. B*, **2001**, *105*(51), 12816.

61. Yan, E.C.Y.L., Y.; Eisenthal, K. B.; *J. Phys. Chem. B*, **2001**, *105*(36), 8531.

62. Zhuang, X., Miranda, P.B., Kim, D., and Shen, Y.R.; *Physical Review B: Condensed Matter and Materials Physics*, **1999**, *59*(19), 12632.

63. Mitchell, S.A.M., R. A.; *J. Phys. Chem. B*, **2004**, *108*(3), 1020.

64. Berkovic, G., Rasing, T., and Shen, Y.R.; *J. Chem. Phys.*, **1986**, *85*(12), 7374.

65. Hanken, D.G., Naujok, R.R., Gray, J.M., and Corn, R.M.; *Anal. Chem.*, **1997**, *69*(2), 240.

66. Flory, W.C., Mehrens, S.M., and Blanchard, G.J.; *J. Am. Chem. Soc.*, **2000**, *122*(33), 7976.

67. Bakiamoh, S.B. and Blanchard, G.J.; *Langmuir*, **2001**, *17*(11), 3438.

68. Bakiamoh, S.B. and Blanchard, G.J.; *Langmuir*, **2002**, *18*(16), 6246.

69. Koos, D.A., Shannon, V.L., and Richmond, G.L.; *Physical Review B: Condensed Matter and Materials Physics*, **1993**, *47*(8), 4730.

70. Lagugne-Labarthet, F., Yu, T., Barger, W.R., Shenoy, D.K., Dalcanale, E., and Shen, Y.R.; *Chem. Phys. Lett.*, **2003**, *381*(3,4), 322.

71. Masahito, O.-e., Hong, S.-C., and Shen, Y.R.; *Molecular Crystals and Liquid Crystals*, **2004**, *412*(1949.

72. Simpson, G.J., Westerbuhr, S.G., and Rowlen, K.L.; *Anal. Chem.*, **2000**, *72*(5), 887.

73. Kikteva, T., Star, D., Zhao, Z., Baisley, T.L., and Leach, G.W.; *J. Phys. Chem. B*, **1999**, *103*(7), 1124.

74. Morgenthaler, M.J.E.M., S. R.; *J. Phys. Chem.*, **1996**, *100*(9), 3323.

75. Hillary, P.J.C., R. M.; *Journal of Physical Chemistry, B*, **1997**, *101*(4494.

76. Kikteva, T.S., D.; Leach, G. W.; *Journal of Physical Chemistry, B*, **2000**, *104*(2860.

77. Salafsky, J.S.E., K.B.; *Chem. Phys. Lett.*, **2000**, *319*(5-6), 435.

78. Simpson, G.J. and Rowlen, K.L.; *J. Am. Chem. Soc.*, **1999**, *121*(11), 2635.

79. Clays, K. and Coe, B.J.; *Chem. Mater.*, **2003**, *15*(3), 642.

80. Attias, A.-J., Cavalli, C., Lemaitre, N., Cherioux, F., Maillotte, H., Ledoux, I., and Zyss, J.; *Journal of Optics A: Pure and Applied Optics*, **2002**, *4*(6), S212.

81. Chaumel, F., Jiang, H., and Kakkar, A.; *Chem. Mater.*, **2001**, *13*(10), 3389.

82. Thayumanavan, S., Mendez, J., and Marder, S.R.; *J. Org, Chem.*, **1999**, *64*(12), 4289.

83. Salafsky, J.S.; *Chem. Phys. Lett.*, **2001**, *342*(5,6), 485.

84. Gannaway, J.N. and Sheppard, C.J.R.; *Optical and Quantum Electronics*, **1978**, *10*(5), 435.

85. Tey, S.H., Prasad, K., Tee, K.C., Chan, L.H., and Seebauer, E.G.; *Thin Solid Films*, **2004**, *466*(1-2), 217.

86. Allen, C.E. and Seebauer, E.G.; *Langmuir*, **1995**, *11*(1), 186.

87. Suni, I.I. and Seebauer, E.G.; *J. Chem. Phys.*, **1994**, *100*(9), 6772.

88. Schultz, K.A., Suni, I.I., and Seebauer, E.G.; *Journal of the Optical Society of America B: Optical Physics*, **1993**, *10*(3), 546.

89. Schultz, K.A. and Seebauer, E.G.; *J. Chem. Phys.*, **1992**, *97*(9), 6858.

90. Johal, M.S., Parikh, A.N., Lee, Y., Casson, J.L., Foster, L., Swanson, B.I., McBranch, D.W., Li, D.Q., and Robinson, J.M.; *Langmuir*, **1999**, *15*(4), 1275.

91. Smilowitz, L., Jia, Q.X., Yang, X., Li, D.Q., McBranch, D., Buelow, S.J., and Robinson, J.M.; *J. Appl. Phys.*, **1997**, *81*(5), 2051.

92. Schaller, R.D., Roth, C., Raulet, D.H., and Saykally, R.J.; *J. Phys. Chem. B*, **2000**, *104*(22), 5217.

93. Schaller, R.D., Johnson, J.C., and Saykally, R.J.; *Anal. Chem.*, **2000**, *72*(21), 5361.

94. Florsheimer, M., Bootsmann, M.-T., and Fuchs, H.; *Adv. Mater. (Weinheim, Ger.)*, **2000**, *12*(24), 1918.

95. Moreaux, L., Sandre, O., and Mertz, J.; *Journal of the Optical Society of America B: Optical Physics*, **2000**, *17*(10), 1685.

96. Campagnola, P.J., Wei, M.-D., Lewis, A., and Loew, L.M.; *Biophys. J.*, **1999**, *77*(6), 3341.

97. Johnson, J.C., Yan, H., Schaller, R.D., Petersen, P.B., Yang, P., and Saykally, R.J.; *Nano Letters*, **2002**, *2*(4), 279.

98. Floersheimer, M., Paschotta, R., Kubitschek, U., Brillert, C., Hofmann, D., Heuer, L., Schreiber, G., Verbeck, C., Sohler, W., and Fuchs, H.; *Appl. Phys. B: Lasers and Optics*, **1998**, *B67*(5), 593.

99. Wiseman, P.W. and Petersen, N.O.; *Biophys. J.*, **1999**, *76*(2), 963.

100. Neuberth, U., Walter, L., von Freymann, G., Schimmel, T., Wegener, M., Khitrova, G., and Gibbs, H.M.; *Appl. Phys. Lett.* , **2002**, *81*(10), 1881.

101. Goldbeck-Wood, G., Bliznyuk, V.N., Burlakov, V., Assender, H.E., Briggs, G.A.D., Tsukahara, Y., Anderson, K.L., and Windle, A.H.; *Macromolecules*, **2002**, *35*(13), 5283.

102. Bischoff, M.M.J., Yamada, T.K., and van Kempen, H.; *Physical Review B: Condensed Matter and Materials Physics*, **2003**, *67*(16), 165403/1.

Chapter 2

DESIGN OF SECOND HARMONIC MICROSCOPY INSTRUMENT, RESULTING INSTRUMENTAL PARAMETERS, AND IMAGE ANALYSIS PROTOCOL

SUMMARY

This chapter details the design and construction of a second harmonic microscopy instrument for the acquisition of surface images. Instrumental parameters such as signal-to-noise ratio, depth of field, and dynamic range are discussed along with the general procedural aspects of image acquisition. We use a Q-switched, mode-locked Nd:YAG laser to produce ~1W average power at the fundamental wavelength of 1064 nm, and we collect the second harmonic at 532nm with a liquid nitrogen cooled CCD camera. The protocol for image analysis, including the Mathematica 4.1 code used for calculation of the autocorrelation function, is also outlined.

2.1 Introduction

Second harmonic generation (SHG) has been successfully used to study a variety of interfacial systems due to the inherent surface selectivity of second order nonlinear processes.[1-14] The origin of this surface selectivity lies in the way the electric field interacts with a molecule. When an electric field is incident on a molecule it induces a polarization response in that molecule dependent on the intensity of the electric field. For low electric field intensities, the resulting polarization response is linear. At high intensity electric field strengths, however, the induced polarization response is nonlinear and, within the dipole approximation, can be represented as a power series expansion in the electric field, E.

$$P = \alpha E + \beta EE^* + \gamma EE^*E + \ldots \qquad (2.1)$$

In equation (2.1) α is the polarizability, β the first hyperpolarizability (or second-order nonlinear coefficient), and γ the second hyperpolarizability (or third order nonlinear coefficient).

Consider the two molecules shown in Figure 2.1 subject to an incident electric field. One contains a center of inversion (left) and the other is without inversion symmetry (right) where *A* and *D* indicate the presence of an electron acceptor and an electron donor, respectively. The net polarization response is determined by the difference in contributions from the positive and negative going portions of the electric field; $P_{net} = P_+ - P_-$. All molecules exhibit a first order polarization response and the susceptibility α is the polarizability familiar from linear optical techniques such as

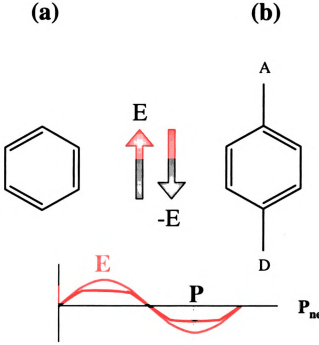

	1st Order	2nd Order	3rd Order
Centro-symmetric System	$P^{(1)}_+ = \alpha E$ $P^{(1)}_- = -\alpha E$ $P^{(1)}_{net} = 2\alpha E$ $\neq 0$	$P^{(2)}_+ = \beta E^2$ $P^{(2)}_- = \beta(-E)^2$ $P^{(2)}_{net} = (\beta - \beta)E^2$ $= 0$	$P^{(3)}_+ = \gamma E^3$ $P^{(3)}_- = \gamma(-E)^3$ $P^{(3)}_{net} = 2\gamma E^3$ $\neq 0$
Non-Centro-symmetric System	$P^{(1)}_+ = \alpha_+ E$ $P^{(1)}_- = -\alpha_- E$ $P^{(1)}_{net} = (\alpha_+ + \alpha_-)E$ $\neq 0$	$P^{(2)}_+ = \beta_+ E^2$ $P^{(2)}_- = \beta_-(-E)^2$ $P^{(2)}_{net} = (\beta_+ - \beta_-)E^2$ $\neq 0$	$P^{(3)}_+ = \gamma_+ E^3$ $P^{(3)}_- = \gamma_-(-E)^3$ $P^{(3)}_{net} = (\gamma_+ + \gamma_-)E^3$ $\neq 0$

Figure 2.1: First, second, and third order polarization responses for **(a)** a centrosymmetric and **(b)** a non-centrosymmetric molecule. Note that for 2nd order processes there is no net polarization response for centrosymmetric molecules.

spontaneous Raman scattering. In contrast, not all molecules will exhibit a second order polarization response. For the molecule in Figure 2.1 having a center of inversion, the net polarization response induced by the electric field is *independent* of field polarity. As a consequence, the second order polarization response will go to zero because β has the same magnitude for either direction of the electric field. In the case of the molecule *lacking* a center of inversion, the polarization response is *dependent* on the direction of the electric field so that β_+ and β_- will have different magnitudes for the positive and negative directions of the electric field. *Because there is a difference in* $P_{net}^{(2)}$, *second order nonlinear processes have the ability to differentiate between molecules with and without a center of inversion.* Like the first order response, all molecules will also exhibit a nonzero third order polarization response. Since the third order response involves E^3, any dependency on the sign of the electric field is removed so that even molecules with a center of inversion have a net third order polarization response that is nonzero.

The symmetry properties discussed above have important consequences for bulk materials since the microscopic polarization response has a macroscopic analog. For bulk materials, the polarization response is described by

$$P = \chi^{(1)}E + \chi^{(2)}EE^* + \chi^{(3)}EE^*E + \ldots \qquad (2.2)$$

where $\chi^{(i)}$ are the optical susceptibilities of the material and correspond to α, β, and γ. Since the properties of bulk materials depend on their microscopic components, the same symmetry constraints derived for the microscopic coefficients also apply to the macroscopic susceptibilities $\chi^{(i)}$. Second-order nonlinear processes are therefore especially suited to the investigation of interfaces because they are free from interference

from the centrosymmetric bulk and, in principle, sense only the interfacial environment.[15] Although generally smaller than $\chi^{(2)}$, the third order nonlinear optical susceptibility, $\chi^{(3)}$, gives rise to a variety of frequency mixing and intensity-dependent refractive index phenomena. Examples of these phenomena include third harmonic generation, coherent Raman effects, and degenerate four-wave mixing. Because $\chi^{(3)}$ is a fourth rank tensor, it has three independent non-zero elements even for isotropic systems[16] and is therefore not suitable for interfacial analyses.

With the introduction of nonlinear optical microscopy, the utility of SHG has been extended even further.[17-28] Second harmonic signal generated from the interface is used as the contrast mechanism for image formation, making information on nonlinear optical chromophore distribution at the surface available. Extracting that information, beyond generating the image itself, is non-trivial since images vary not only from sample to sample but also between different regions of the same sample. In an effort to extract comparable information from a variety of samples (or from a variety of regions within the same sample) we propose an autocorrelation approach, the details of which are described in section 2.5.

2.2 Modification of Existing SSHG Instrument

For the experiments described herein, the second harmonic microscopy instrument was built in-house by modifying the existing surface second harmonic generation (SSHG) instrument, previously used to conduct SSHG intensity experiments. The Q-switched, mode locked Nd:YAG laser (Quantronix 416, 100 ps mode-locked

pulses, 12 ns interpulse spacing, 500Hz Q-switch frequency) produces fundamental output at 1064nm, with ~1W average power at the sample. Primary modifications to the SSHG intensity instrument were the introduction of a microscope objective to the optics train and the substitution of a liquid nitrogen (LN_2) cooled charge couple device (CCD) camera for the photomultiplier tube (PMT) detector.

Figure 2.2 illustrates the instrumental set-up. IR output was directed through a beamsplitter and the two beams focused onto the sample surface. Note the non-collinear beam geometry, which provides further spatial resolution of the resultant second harmonic from the fundamental. For monolayer experiments, second harmonic light (532nm) generated from the surface was collected with a 100x microscope objective (Mitutoyo M Plan Apo SL100) having numerical aperture (NA) 0.55 and corrected for curvature of field, chromatic, and spherical aberrations. For multilayer experiments a 10x microscope objective was used to collect the resultant second harmonic light (Mitutoyo M Plan Apo SL10, NA=0.28). After being collected by the objective, the second harmonic output was passed through an IR filter (Schott glass BG-39) to remove any residual fundamental IR radiation, and was imaged onto the face of a LN_2 cooled CCD camera (VersArray 700B/LN, Princeton Instruments) using an InfiniTube™ microscope collimation optic assembly.

Because of the crossed beam geometry, the need for an optical delay was a consideration in the instrument design. Figure 2.3 shows the beam path through the optics train, up to the focusing lens. At the beamsplitter, the portion of the beam that is reflected and directed towards the high reflector travels along Arm 1 of the optics train. The portion of the beam that is refracted, and must pass through the beamsplitter, travels

along Arm 2 of the optics train. Total transit time through Arm 1 was determined to be 680ps, using simply the speed of light and the physical distances between optics. For Arm 2, however, the speed of light is modulated as it passes through the beamsplitter according to the refractive index of that medium (BK7 glass, n = 1.506). Using Snell's law to determine the length of the refracted light path and the modulated speed of light through the glass medium, the transit time through the beamsplitter was determined to be 34ps. The total transit time for Arm 2 was then determined to be 664ps, a difference of only 16ps from Arm 1. Since the difference in beam arrival times at the focusing lens was so small, an optical delay was unnecessary.

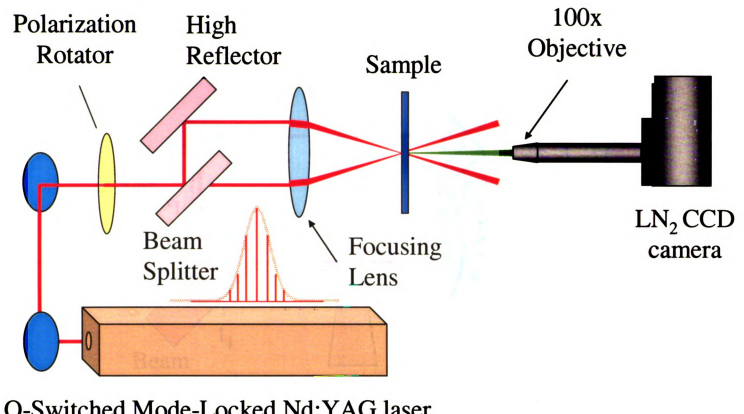

Figure 2.2: Surface second harmonic microscopy instrument with fundamental output of 1064nm. Crossed-beam geometry provides additional spatial filtering.

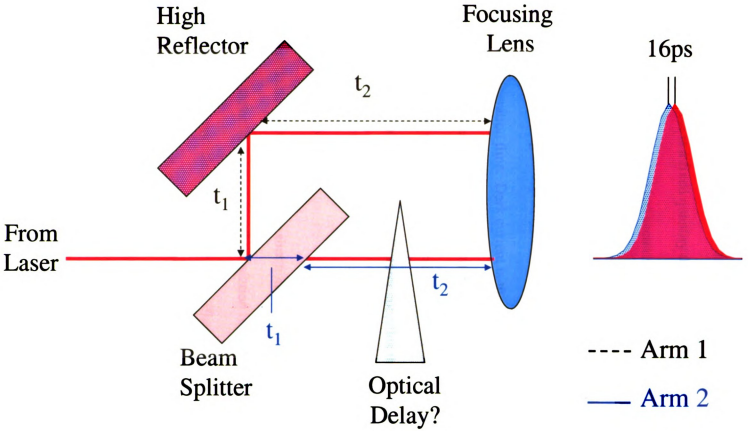

Figure 2.3: Beam transit time through each arm of the optics train. The difference in total transit time through each arm is only 16ps, which is not sufficient to require an optical delay

2.3 Signal to Noise Ratio

The signal-to-noise ratio (SNR) of the imaging instrument is determined by both the laser properties and the camera specifications. We consider the CCD camera first. Two sources of noise inherently arise from the detector itself, dark current and readout noise. Readout noise is a fixed quantity that arises primarily from the output amplifier. In a CCD camera once charge has accumulated in the pixel wells (after exposure to light) that charge is transferred to the serial register and then to the output node. From the output node the charge is amplified by the output amplifier (or preamplifier) and transferred to the analog-to-digital (A/D) converter.[29] Unlike readout noise, dark current varies with integration time. Dark current is the thermally induced generation of charge over time, which is detected by the camera independent of the presence of an illumination source. Dark current noise is the statistical variation of the dark current specification.[30] For the VersArray 700B/LN the manufacturer specifies the readout noise as $3e^{-}$ $pixel^{-1}$ and the dark current as 0.0003 e^{-} pix^{-1} s^{-1}. All experiments were conducted using an integration time of 10 minutes.

In addition to the camera, the shot noise introduced by the laser must also be considered. Shot noise accounts for the variation in photon flux from the laser and arises inherently from the particle like nature of light. Photon shot noise is accounted for in the first term of the denominator of equation 2.3, as the square root of the photon flux.

Quantitatively the signal-to-noise ratio for the camera is described by the following equation: [31]

$$SNR = \frac{I(QE)t}{\sqrt{I(QE)t + N_d t + N_r^2}} \qquad (2.3)$$

where I is the photon flux, QE the quantum efficiency of the camera, t the integration time, N_d the dark current, and N_r the readout noise. Photon flux was calculated to be 0.26 ph/pix/s at the second harmonic wavelength of 532 nm for a Nd:YAG average laser power of ~1W. The quantum efficiency of the camera was also specified by the manufacturer as $QE = 0.85$. According to equation (2.3) SNR = 11. This signal-to-noise ratio is sufficient to differentiate generated second harmonic signal from the noise sources present in the experiment and represents the ratio obtained for a bare substrate containing no $\chi^{(2)}$ –active chromophore. For substrates containing a $\chi^{(2)}$-active molecule (or polymer) the signal would only increase, improving the signal-to-noise ratio even further.

2.4 Resolution, Depth of Field, and Dynamic Range

Resolution

A microscope's optical resolution is determined by its numerical aperture (NA) and the wavelength of light used for illumination. Resolution can be determined through the Rayleigh equation: [32]

$$R = \frac{\lambda}{2NA} \tag{2.4}$$

where R is the optical resolution, NA the numerical aperture of the objective, and λ the wavelength of illumination. For the 100x microscope objective used in the monolayer experiments (NA = 0.55 and λ = 532nm) the resolution was calculated to be 0.5μm. For multilayer experiments, a 10x microscope objective was used (Mitutoyo M Plan Apo SL10) with numerical aperture 0.28. This corresponds to a resolution of 0.9μm.

While the calculations above represent the minimum distance that two features may be separated by and still be resolved, it remains to determine the spatial resolution of the image itself. The spatial resolution, R_s, of a digital image is a function of the pixel size and the magnification of the microscope objective.[33]

$$R_s = \frac{Pixel\ Size\ (\mu m)}{Objective\ Magnification} \tag{2.5}$$

The pixel size for the VersArray 700B/LN camera is 20μm x 20μm and magnifications for the Mitutoyo SL objectives used in this work were 100x and 10x. For images collected with the 100x and 10x microscope objectives, equation 2.5 yields spatial resolutions of 0.20μm and 2.0μm respectively. A spatial resolution value of 0.20μm, for example, means that each pixel of the imaging array corresponds to 0.20μm x 0.20μm area of the sample.

As a general rule the spatial resolution of the image should be two to three times *smaller* than the optical resolution limit of the microscope so that all of the fine structure resolved by the microscope may be captured in the digital image.[33] This rule is derived from the Nyquist theorem (or equivalently the Shannon sampling theorem) which states that a periodic signal must be sampled at greater than or equal to twice its highest frequency component in order to accurately reproduce the original signal from its samples.[34] The optical resolution of the microscope was calculated to be 0.5μm for the 100x objective and 0.9μm for the 10x objective. A spatial resolution of 0.20μm for images acquired with the 100x objective does fall within the guidelines of the general rule stated previously since it is at least half of the optical resolution limit. Images acquired with the 100x objective are therefore limited by the optical resolution and not

the imaging array itself. This means that each pixel in the images taken with the 100x objective represents 0.5μm of the sample area even though the spatial resolution of the imaging array is 0.2μm.

The spatial resolution of 2.0μm calculated for images collected with the 10x microscope objective does not fall within the guidelines since the optical resolution calculated for the 10x objective was only 0.9μm. Such a result simply indicates that for images acquired with the 10x objective resolution is limited by the imaging array of the camera and not by the optics themselves. Therefore, each pixel in the images acquired with the 10x objective represents 2.0μm of the sample area even though the optics can resolve features that are 0.9μm apart.

Depth of Field

While resolution is measured in the plane *perpendicular* to the optical axis, depth of field, *d*, is measured *parallel* to the optical axis. Depth of field is the distance between the nearest and farthest object planes in focus and, like lateral resolution, is dependent on the numerical aperture of the microscope objective and the wavelength of illumination: [35]

$$d = \frac{\lambda\sqrt{n^2 - (NA)^2}}{(NA)^2} \tag{2.6}$$

where n is the refractive index of the medium between the sample and the objective front lens, which is air for our experiments. Calculated depth of field for the 100x objective (NA = 0.55) used in the monolayer imaging studies was 1.5μm. For the 10x objective used in the multilayer studies (NA = 0.28) the depth of field was calculated to be 6.5μm.

Dynamic Range

The dynamic range (DR) of a CCD camera describes its ability to quantitatively measure both very bright spots and very dim spots in the same image; however, illumination is usually a function of the application or dependent upon experimental conditions. Therefore, CCD manufacturers have adopted a definition of dynamic range that is independent of the experimental conditions under which the camera is used. The dynamic range is specified as: [36]

$$DR = \frac{full\ well\ capacity\ (e^-)}{readout\ noise\ (e^-)} \tag{2.7}$$

where the full well capacity is the amount of charge an individual pixel can accumulate before the charge overflows into the next pixel. Full well capacity is based on pixel size so that larger pixels have a higher full well capacity. For the VersArray 700B/LN camera used in this work the pixel size was 20μm x 20μm and the full well capacity 67,000 e^-. For a readout noise of 3 e^- $pixel^{-1}$, the dynamic range for a single pixel is 2.2 x 10^4.

2.5 Image Acquisition

Once a sample was prepared it was mounted in the focal plane of the second harmonic microscopy instrument and the two incident fundamental beams were overlapped at the surface. In order to remove any scattered second harmonic generated from the fundamental beams a flat field correction was applied. One of the incident fundamental beams was blocked and an image acquired using only a single beam to illuminate the sample. This image was then used as the flat field correction file for the

double beam image. Flat field corrections were done prior to each double beam image acquisition in order to account for differences between substrates.

Sample images were collected for both 0° and 90° fundamental beam polarizations (with respect to the optical table surface normal) and all polarizations of the second harmonic were collected. Image acquisition was done at a camera temperature of -106.5°C using a 10 minute acquisition time. Figure 2.4 shows a typical raw surface image. This particular image is of a sample having 60% C1 and 40% HDPA monolayer composition, collected at a fundamental beam polarization of 0°. All images have a false color overlay and a normalized intensity. Note the circular outline of the microscope objective and the region of SHG activity to the right of center. This is the region of the overlapped fundamental beams and is off center due to constraints in positioning the optics train relative to the camera's central viewing axis.

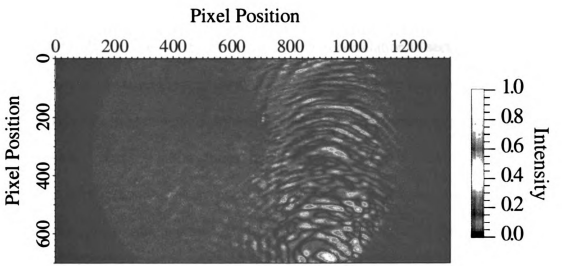

Figure 2.4: Typical raw surface image from the second harmonic microscopy instrument described in section 2.2. The large circular outline is the objective viewable area. Note the region of SH activity is slightly off center.

2.6 Data Processing

Data processing was done post-acquisition, with the difference images generated by subtracting the image collected at 90° polarization rotation from the image collected at 0° polarization rotation. The original .SPE file generated by the WinView software was then converted to ASCII format for further manipulation in OriginPro 7.0. Files imported to Origin consisted of three columns: x-axis pixel position, y-axis pixel position, and the pixel intensity. Pixel position columns were discarded and the intensity column was corrected so that the lowest intensity value was zero. The intensity correction was necessary due to the subtraction of one image from another, which created negative intensity values at some positions of the difference image.

Once the position columns were eliminated and the intensity column corrected in Origin 7.0, the image file was imported to Mathematica 4.1 for numerical calculation of the autocorrelation function. Although the AC functions were calculated numerically, we provide a brief discussion of the mathematics of autocorrelation in section 2.7.

Figure 2.5 shows the Mathematica 4.1 code used for the calculations. First the entire image was imported and graphically rendered. Next, various regions of the image were sampled according to the input parameters of x and y pixel position. Sub-regions of the image were selected using a random number generation program to produce a random ordinate pair. This random ordinate pair was used as the 'origin' of the 100 x 100 pixel sub-region. Once the sub-region was selected, the autocorrelation function was calculated numerically by computing the Fourier transform of the data set, multiplying it by its complex conjugate, then performing an inverse Fourier transform on the resulting product. The autocorrelation function was then saved as a text file and imported back

into Origin for enhanced graphic rendering. Normalization of the autocorrelation function consisted of subtracting the minimum function value from the array, so that its lowest value was set to zero, and then dividing the array by the maximum function value. An example of what the 2D autocorrelation function of an image looks like is shown in Figure 2.6. The AC function shows correlation in the vertical dimension where the most overlap of the letters would occur as the raw image is displaced relative to itself. Also, the amplitude of the autocorrelation function falls away quite rapidly from the origin (exact overlap) indicating that at small displacements from the origin the image is poorly correlated with itself.

```
here =
  SetDirectory[
   "C:\Documents and Settings\Michelle Rini\My Documents\Multilayers\
     Corrected Intensity"];
stream = OpenRead["cB720C2L1diff.TXT"];
data = Table[Read[stream], {i, 1, 700}, {j, 1, 1340}];

ListContourPlot[data, PlotRange → All, ColorFunction → Hue]
```

(Contour plot appears here)

```
(*J is the x-axis index*)
(*I is the y-axis index*)

minJ = 600;
maxJ = 1000;
minI = 200;
maxI = 500;
DATA = Table[sub[x, y] = 0, {x, minJ, maxJ}, {y, minJ, maxJ}];
For[j = minJ, j ≤ maxJ, j++, For[i = minI, i ≤ maxI, i++,
   sub[i, j] = Extract[data, {i, j}]]];
submatrix = Table[sub[i, j] = sub[i, j], {i, minI, maxI}, {j, minJ, maxJ}];

ListContourPlot[submatrix, ColorFunction → Hue]
```

(Contour plot appears here)

```
ft = Re[InverseFourier[Fourier[submatrix] * Conjugate[Fourier[submatrix]]]];

ListContourPlot[ft, PlotRange → All, ColorFunction → Hue]
```

(Contour plot appears here)

```
there =
  SetDirectory[
   "C:\Documents and Settings\Michelle Rini\My Documents\Multilayers\
     Mathematica Output"];
OpenWrite["ftcAC2L1diff.TXT"];
Write["ftcAC2L1diff.txt", ft]
Close["ftcAC2L1diff.txt"]
```

Figure 2.5: Mathematica code used in autocorrelation calculation.

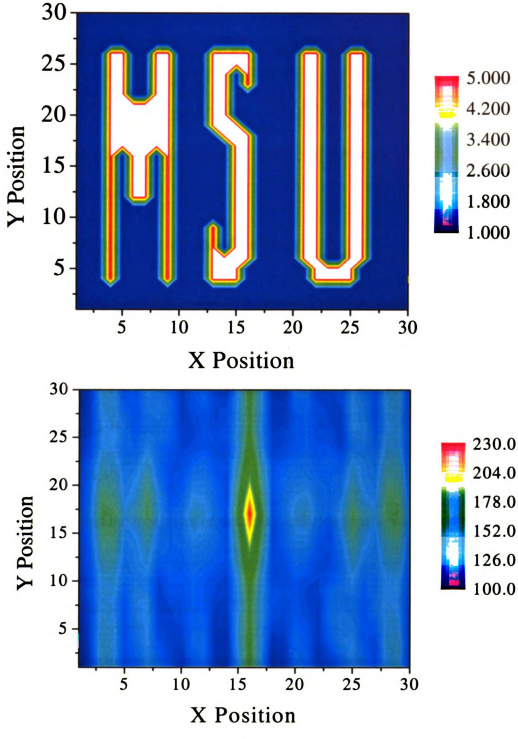

Figure 2.6: Sample image (top panel) and the associated autocorrelation function (bottom panel)

2.7 Autocorrelation Function Calculation

For a two-dimensional function *f(x,y)*, the autocorrelation function is given by:

$$C(x,y) = f(x,y) \otimes f(x,y) = \int_{-\infty}^{\infty}\int_{-\infty}^{\infty} f(x',y')f(x+x',y+y')dx'dy' \tag{2.8}$$

The autocorrelation theorem states that: If $\Im\{f(x,y)\} = F(u,v)$, where $\Im$ is the Fourier transform of *f(x,y)*, then:

$$\Im\left\{\int_{-\infty}^{\infty}\int_{-\infty}^{\infty} f(x',y')f(x+x',y+y')dx'dy'\right\} = |F(u,v)|^2 \tag{2.9}$$

where $|F(u,v)|^2$ is the power spectrum of the image. This relationship is quite advantageous since calculation of the Fourier transform of the image is straightforward. Once the term $|F(u,v)|^2$ is evaluated, the autocorrelation function can be obtained by back transformation.[34, 37]

$$C(x,y) = \Im^{-1}\left\{|F(u,v)|^2\right\} \tag{2.10}$$

It can be shown that the maximum of the autocorrelation function occurs at the origin, or that:

$$\int_{-\infty}^{\infty} f(u)f(u+x)du \leq \int_{-\infty}^{\infty} f^2(u)du \tag{2.11}$$

To verify the above expression, let ε be a real number. Then:

$$\int_{-\infty}^{\infty} \{f(u)+\varepsilon f(u+x)\}^2 du > 0 \tag{2.12}$$

expanding the quadratic yields the expression:

$$\int_{-\infty}^{\infty} f^2(u)du + 2\varepsilon\int_{-\infty}^{\infty} f(u)f(u+x)du + \varepsilon^2\int_{-\infty}^{\infty} f^2(u+x)du > 0 \tag{2.13}$$

$$\int_{-\infty}^{\infty} f^2(u)du + 2\varepsilon \int_{-\infty}^{\infty} f(u)f(u+x)du + \varepsilon^2 \int_{-\infty}^{\infty} f^2(u)du > 0 \qquad (2.14)$$

Now, let a and b have the following definitions:

$$a \equiv \int_{-\infty}^{\infty} f^2(u)du \qquad b \equiv 2\int_{-\infty}^{\infty} f(u)f(u+x)du \qquad (2.15)$$

Equation 2.8 then becomes: $a\varepsilon^2 + b\varepsilon + a > 0$. Since this quadratic equation does not have a real root, $b^2 - 4a^2 \leq 0$, or $b/2 \leq a$. Using the definitions of 2.9

$$\int_{-\infty}^{\infty} f(u)f(u+x)du \leq \int_{-\infty}^{\infty} f^2(u)du \qquad (2.16)$$

with the equality occurring at x = 0.[38]

Several examples of autocorrelation analysis can be found in the literature.[39-45] Neuberth et al. have used a two dimensional (2D) autocorrelation analysis to examine nanophotoluminescence images of GaAs quantum wells grown on a (100) GaAs substrate. Background correction was performed on the raw photoluminescence images by subtracting the average intensity. The 2D spatial autocorrelation function was calculated directly from equation 2.8, without transformation to the frequency domain, and computed AC functions were averaged until acceptable statistics were achieved.[40]

Petersen and co-workers used a slightly different method than that of Neuberth to study the distribution of membrane receptors on human fibroblasts. Confocal scanning micrographs of the visualized receptors were obtained and a normalized spatial autocorrelation function for a discrete set of points calculated directly according to the following equation:

$$g(\xi,\eta) = \frac{(1/NM)\sum_{k=1}^{N}\sum_{l=1}^{M} i(k,l)\,i(k+\xi,l+\eta)}{[(1/NM)\sum_{k=1}^{N}\sum_{l=1}^{M} i(k,l)]^2} \quad - \quad 1 \qquad (2.17)$$

where i indicates intensity. The variables ξ and η simply represent the in plane spatial displacement coordinates. Equation 2.17 was used to evaluate the term *g(0,0)* as a measure of the density of fluorescent particles present in the image. As an alternative to direct computation of the spatial AC function, Petersen also described the Fourier transform method of equations 2.9 and 2.10 for determination of the numerator of equation 2.17.[44] Since we are not interested in explicitly evaluating the *g(0,0)* term, our normalization procedure varies from that described by equation 2.17 and was described in section 2.6.

Line Profiles and Peak Area Ratio

To evaluate the characteristic persistence length of chromophore aggregation on the surface, a line profile through the highest correlation amplitude was extracted from the two-dimensional autocorrelation function. The line profile expresses the normalized correlation amplitude as a function of x-axis pixel position. Once the line profile was generated, its full width at half maximum (FWHM) was determined (in pixels) and converted to distance. For each sample twenty line profiles were extracted from twenty different autocorrelation functions, and then averaged. The line profiles appeared to exhibit a superposition of two distinct lineshapes. At high chromophore loading density the line profiles were broad with a small, narrow spike at the top while at loading densities below 50% the narrow component was more prominent. The FWHM values recovered from line profiles of both the broad and narrow components and their relative contributions to the total peak area will be discussed in chapter 3. The ratio of the narrow peak area to the total peak area was then calculated using a Gaussian line fitting protocol. Using the nonlinear curve fitting tool in OriginPro 7.0, the broad Gaussian component was fit first by adjusting the fitting width and amplitude input parameters. The broad Gaussian fit was then subtracted from the experimental data to isolate the narrow component of the line profile. This narrow component was fit independently and the peak area estimates for both components obtained from their respective fits. Figure 2.7 illustrates the two component Gaussian fit (broad component in red, narrow component in green) and the overall fit to the experimental data (blue).

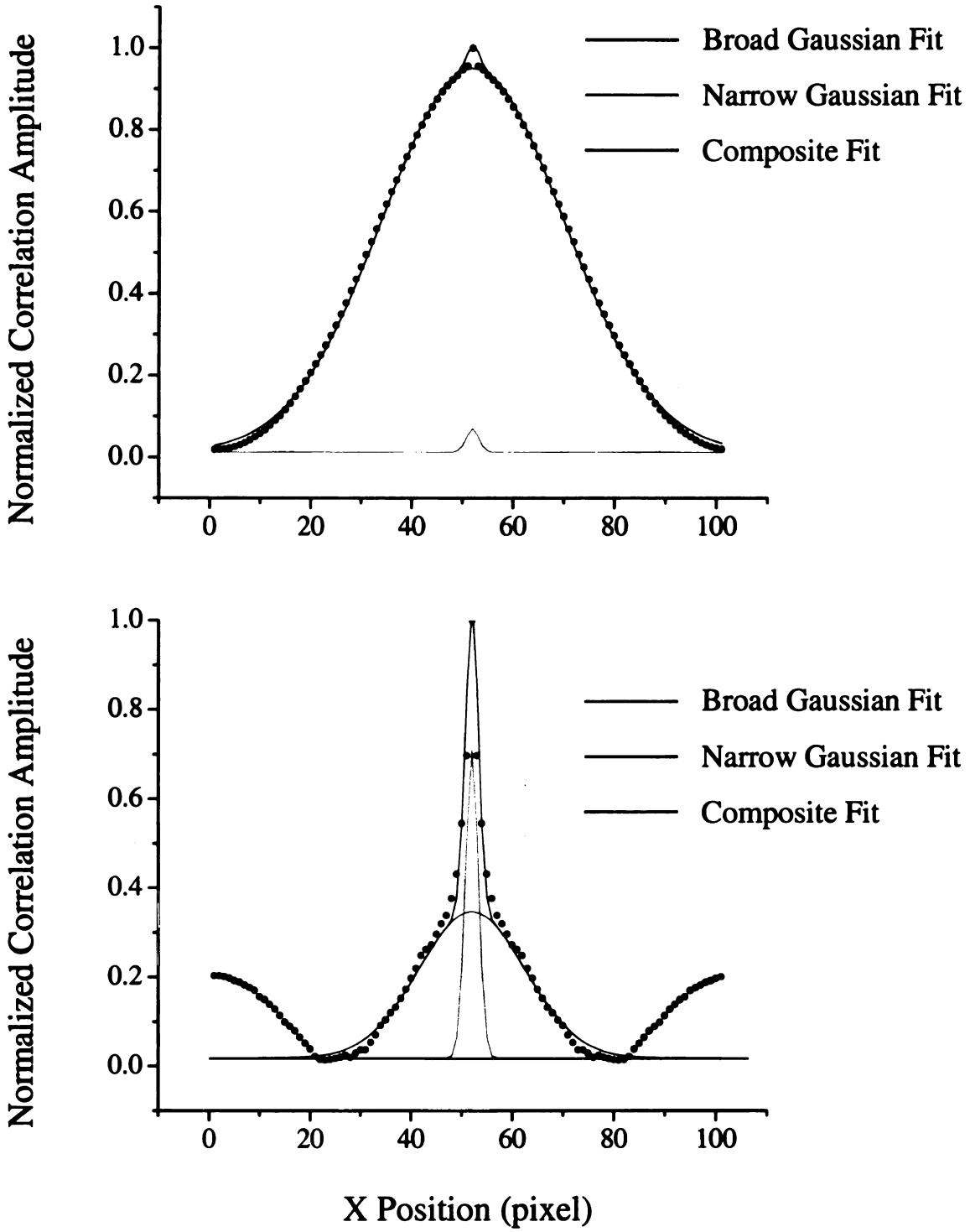

Figure 2.7: Example of peak area fitting for image line profiles. Top panel represents an area taken from a 60% C1 sample and the bottom panel a region from a 50%C1 sample.

2.8 Conclusions

We have designed and built a second harmonic microscopy instrument in order to acquire images of nonlinear chromophore distributions on a nominally amorphous surface. We have also developed an analysis protocol to extract the characteristic domain sizes of surface features. This analysis protocol utilizes the relationship between spatial correlation and the frequency domain, allowing fast numerical calculation of the autocorrelation function.

Images in this thesis are presented in color and may not translate accurately to black and white

2.8 Literature Cited

1. Simpson, G.J. and Rowlen, K.L.; *Anal. Chem.*, **2000**, *72*(15), 3407.

2. Simpson, G.J.; *Appl. Spectrosc.*, **2001**, *55*(1), 16A.

3. Shen, Y.R.; *Surf. Sci.*, **1994**, *299-300*(1-3), 551.

4. Nuzzo, R.G., Fusco, F.A., and Allara, D.L.; *J. Am. Chem. Soc.*, **1987**, *109*(8), 2358.

5. Shannon, V.L.K., D.A.; Richmond, G.L; *Appl. Opt.*, **1987**, *26*(17), 3579.

6. Salafsky, J.S.E., K.B.; *Chem. Phys. Lett.*, **2000**, *319*(5-6), 435.

7. Kott, K.L., Higgins, D.A., McMahon, R.J., and Corn, R.M.; *J. Am. Chem. Soc.*, **1993**, *115*(12), 5342.

8. Katz, H.E., Wilson, W.L., and Scheller, G.; *J. Am. Chem. Soc.*, **1994**, *116*(15), 6636.

9. Higgins, D.A.A., M.B.; Byerly, S.K.; Corn, R.M.; *Langmuir*, **1992**, *8*(8), 1994.

10. Higgins, D.A., Byerly, S.K., Abrams, M.B., and Corn, R.M.; *J. Phys. Chem.*, **1991**, *95*(18), 6984.

11. Heinz, T.F., Chen, C.K., Ricard, D., and Shen, Y.R.; *Chem. Phys. Lett.*, **1981**, *83*(1), 180.

12. Han, S.H., Belkin, M.A., and Shen, Y.R.; *Opt. Lett.*, **2004**, *29*(13), 1527.

13. Corn, R.M. and Higgins, D.A.; *Chem. Rev.*, **1994**, *94*(1), 107.

14. Brudny, V.L., Mendoza, B.S., and Luis Mochan, W.; *Physical Review B: Condensed Matter and Materials Physics*, **2000**, *62*(16), 11152.

15. Prasad, P.N.W., D.J, Introduction to Nonlinear Optical Effects in Molecules and Polymers. 1 ed. 1991, John Wiley & Sons, New York.

16. Prasad, P.N. Third-Order Nonlinear Optical Effects in Molecular and Polymeric Materials. In *Materials for Nonlinear Optics: Chemical Perspectives*, Marder, S.R., Sohn, J.E., Stucky, G.D.; ACS Symposium Series; American Chemical Society: Washington D.C, 1991; 50.

17. Campagnola, P.J., Wei, M.-D., Lewis, A., and Loew, L.M.; *Biophys. J.*, **1999**, *77*(6), 3341.

18. Floersheimer, M., Paschotta, R., Kubitschek, U., Brillert, C., Hofmann, D., Heuer, L., Schreiber, G., Verbeck, C., Sohler, W., and Fuchs, H.; *Appl. Phys. B: Lasers and Optics*, **1998**, *B67*(5), 593.

19. Florsheimer, M.; *Phys. Status Solidi A*, **1999**, *173*(1), 15.

20. Florsheimer, M., Bosch, M., Brillert, C., Wierschem, M., and Fuchs, H.; *J. Vac. Sci. Technol., B*, **1997**, *15*(4), 1564.

21. Johnson, J.C., Yan, H., Schaller, R.D., Petersen, P.B., Yang, P., and Saykally, R.J.; *Nano Letters*, **2002**, *2*(4), 279.

22. Mishina, E.D., Sherstyuk, N.E., Vorotilov, K.A., Sigov, A.S., Barberi, R., Moret, M.P., Manders, F., De Santo, M.P., Larsen, P.K., and Rasing, T.; *Appl. Phys. B: Lasers and Optics*, **2002**, *74*(7-8), 783.

23. Moreaux, L., Sandre, O., and Mertz, J.; *Journal of the Optical Society of America B: Optical Physics*, **2000**, *17*(10), 1685.

24. Rechsteiner, P., Hulliger, J., and Floersheimer, M.; *Chem. Mater.*, **2000**, *12*(11), 3296.

25. Schaller, R.D., Johnson, J.C., and Saykally, R.J.; *ChemPhysChem*, **2003**, *4*(11), 1243.

26. Schaller, R.D., Johnson, J.C., Wilson, K.R., Lee, L.F., Haber, L.H., and Saykally, R.J.; *J. Phys. Chem. B*, **2002**, *106*(20), 5143.

27. Schaller, R.D., Roth, C., Raulet, D.H., and Saykally, R.J.; *J. Phys. Chem. B*, **2000**, *104*(22), 5217.

28. Smilowitz, L., Jia, Q.X., Yang, X., Li, D.Q., McBranch, D., Buelow, S.J., and Robinson, J.M.; *J. Appl. Phys.*, **1997**, *81*(5), 2051.

29. Reed Business Information/Test & Measurement World; Titus, J., *How do CCDs Capture Images?*, http://www.reed-electronics.com/tmworld/article/CA187479.html, Accessed 02/21/05.

30. Roper Scientific Home Page/Library/Encyclopedia; *Dark Current*, http://www.princetoninstruments.com/library_enc_dark.shtml, Accessed 2/21/05.

31. Roper Scientific Home Page/Library/Encyclopedia; *Signal-to-Noise Ratio*, http://www.princetoninstruments.com/library_encyclopedia.shtml, Accessed 02/14/05.

32. Olympus America Inc.; Abramowitz, M.D., M.W., *Numerical Aperture and Resolution*, http://www.olympusmicro.com/primer/anatomy/numaperture.html, Accessed 01/26/05.

33. Olympus BioSystems; *Camera Resolution*, http://www.olympus-biosystems.com/templates_eng/bio_imaging/glossary_resolution.html, March 2005.

34. Bracewell, R.N., The Fourier Transform and Its Applications. 3 ed. 2000, McGraw-Hill, New York.

35. Olympus America Inc.; Abramowitz, M.D., M.W., *Depth of Field and Image Depth*, http://www.olympusmicro.com/primer/anatomy/focusdepth.html, Accessed 01/26/05.

36. Roper Scientific Home Page/Library/Encyclopedia; *Dynamic Range*, http://www.princetoninstruments.com/library_encyclopedia.shtml, Accessed 2/14/05.

37. Goodman, J.W., Introduction to Fourier Optics. 1968, McGraw-Hill, New York.

38. Mathworld -- A Wolfram Web Resource; Weisstein, E.W., *Autocorrelation*, http://mathworld.wolfram.com/Autocorrelation.html,

39. Wiseman, P.W. and Petersen, N.O.; *Biophys. J.*, **1999**, *76*(2), 963.

40. Neuberth, U., Walter, L., von Freymann, G., Schimmel, T., Wegener, M., Khitrova, G., and Gibbs, H.M.; *Appl. Phys. Lett.* , **2002**, *81*(10), 1881.

41. Goldbeck-Wood, G., Bliznyuk, V.N., Burlakov, V., Assender, H.E., Briggs, G.A.D., Tsukahara, Y., Anderson, K.L., and Windle, A.H.; *Macromolecules*, **2002**, *35*(13), 5283.

42. Bischoff, M.M.J., Yamada, T.K., and van Kempen, H.; *Physical Review B: Condensed Matter and Materials Physics*, **2003**, *67*(16), 165403/1.

43. Tokumasu, F., Hwang, J., and Dvorak, J.A.; *Langmuir*, **2004**, *20*(3), 614.

44. Petersen, N.O., Hoeddelius, P.L., Wiseman, P.W., Seger, O., and Magnusson, K.E.; *Biophys. J.*, **1993**, *65*(3), 1135.

45. Hwang, J., Gheber, L.A., Margolis, L., and Edidin, M.; *Biophys. J.*, **1998**, *74*(5), 2184.

Chapter 3

C1 MONOLAYER STUDIES: THE EFFECT OF MONOLAYER COMPOSITION ON SURFACE DISTRIBUTION

SUMMARY

We report here on the characteristic domain sizes observed for monolayers comprised of the nonlinear chromophore C1. Monolayer compositions ranged from 0% to 100% chromophore where concentration was controlled with the diluent molecule HDPA. Autocorrelation analyses indicate that two domains are present on the surface and their estimated their sizes are ~15μm and ~1μm. Due to the resolution limits of the second harmonic microscopy instrument, it is not clear whether the ~1μm domain is comprised of a single domain or many smaller domains.

3.1 Introduction

Recently, second harmonic generation (SHG) has emerged as a powerful tool for surface characterization.[1-3] While SHG intensity experiments have provided a wealth of information on interfacial systems, that information is averaged over the illuminated spot size and therefore provides no information about chromophore *distribution.* In an effort to obtain local information on molecular order and orientation, second harmonic generation has been successfully coupled with microscopy. A variety of systems have been imaged using second harmonic microscopy (SHM) including biological membranes and red blood cells,[4-7] ferroelectric domains in inorganic crystals,[8-11] poled silica waveguides,[12] and LB films.[13, 14]

Flörsheimer *et al.* have done considerable work in both the imaging of ferroelectric domains in NLO crystals and the imaging of LB films. In the NLO crystal studies, the ferroelectric domains of poled crystals of $LiNbO_3$ and $LiTaO_3$ were imaged. Second harmonic micrographs of various faces of the crystals were obtained and the domain walls were clearly visible. Inverted domains appeared as filament-like structures and provided a qualitative assessment of domain structure. The main focus of these crystal studies, however, was using SHM as a rapid, nondestructive gauge of the success of the poling process, as evidenced by the appearance of the inverted domains, and not the size of the domains themselves.[8, 9]

In their work on Langmuir-Blodgett films, Flörsheimer and co-workers imaged monolayers of 12-N-methyl-N-((7-nitrobenz-2-oxadiazol-4-yl)amino) octadecanoic acid (S-NBD) and 2-docosylamino-5-nitropyridine (DCANP), spread onto a liquid surface. For the monolayer of S-NBD the crystalline and fluid phases of the film were coexistent

and the bright, needle like structures exhibited in the SH micrographs were attributed to the solid domains within the film.[13]

Like the monolayer of S-NBD, SH micrographs of a monolayer of DCANP also exhibited clearly defined features. Irregular, dendridic structures were observed in images of the DCANP monolayer and the contrast mechanism was described generally as a lateral variation of molecular order and arrangement. More specifically, it was assumed that local structural features had the same (or similar) symmetry and order and were therefore governed by the same susceptibility tensor. Then the contrast could be explained as a variation in the effective nonlinear susceptibility due to orientational variations in the crystallographic axes.[14] Despite the successful imaging of LB films and a description of the contrast mechanism, domain sizes within the films themselves were not addressed.

Although second harmonic microscopy has been successfully used to image surfaces, information beyond acquiring the image itself is not widely available. Autocorrelation analysis has been used previously to assess domain sizes, but it has not been widely applied to the analysis of nonlinear microscopy images.[15-18] We are interested in combining the power of an autocorrelation analysis with the ability to acquire surface images in order to investigate domain size on an amorphous, dielectric surface.

3.2 Experimental

Surface images were acquired for monolayer compositions of the nonlinear optical chromophore (4-(4-(4-(4-((2-Hydroxyethyl) sulfonyl) phenyl) piperazinyl)-phenyl) phosphonic acid (**C1**) ranging from 10-100% chromophore. Figure 3.1 shows the structure of C1 along with the diluent molecule 1-hydroxyl-12-dodecylphosphonic acid (**HDPA**) used to control the composition of C1 in the monolayer. The nonlinear chromophore C1 has been reported previously by Katz et. al.[19] and exhibits a 'push-pull' type structure with the piperazinyl- group acting as an electron donating source, across the conjugated azo-bridge, to the sulfonyl- group, which acts as an electron withdrawing group.

Monolayer samples of C1 were prepared by cleaning quartz substrates in piranha solution (3:1 sulfuric acid: hydrogen peroxide; ***caution, strong oxidizer***) for 15 minutes followed by rinsing with distilled water and then drying under a nitrogen stream. The substrates were then phosphorylated, under inert atmosphere, in a solution of acetonitrile (10mL), 2,4,6-collidine (0.3M), and phosphorousoxychloride (0.3M). Immersion time for phosphorylation was 30 minutes after which, the samples were rinsed first with reagent grade acetonitrile, then water, and dried under nitrogen. Following phosphorylation, the samples were immersed in a 10mM solution of $ZrOCl_2$ for 15 minutes, rinsed with water and dried. Finally, the samples were immersed in the appropriate solution of C1 and HDPA and heated to ~50°C for 1 hour.

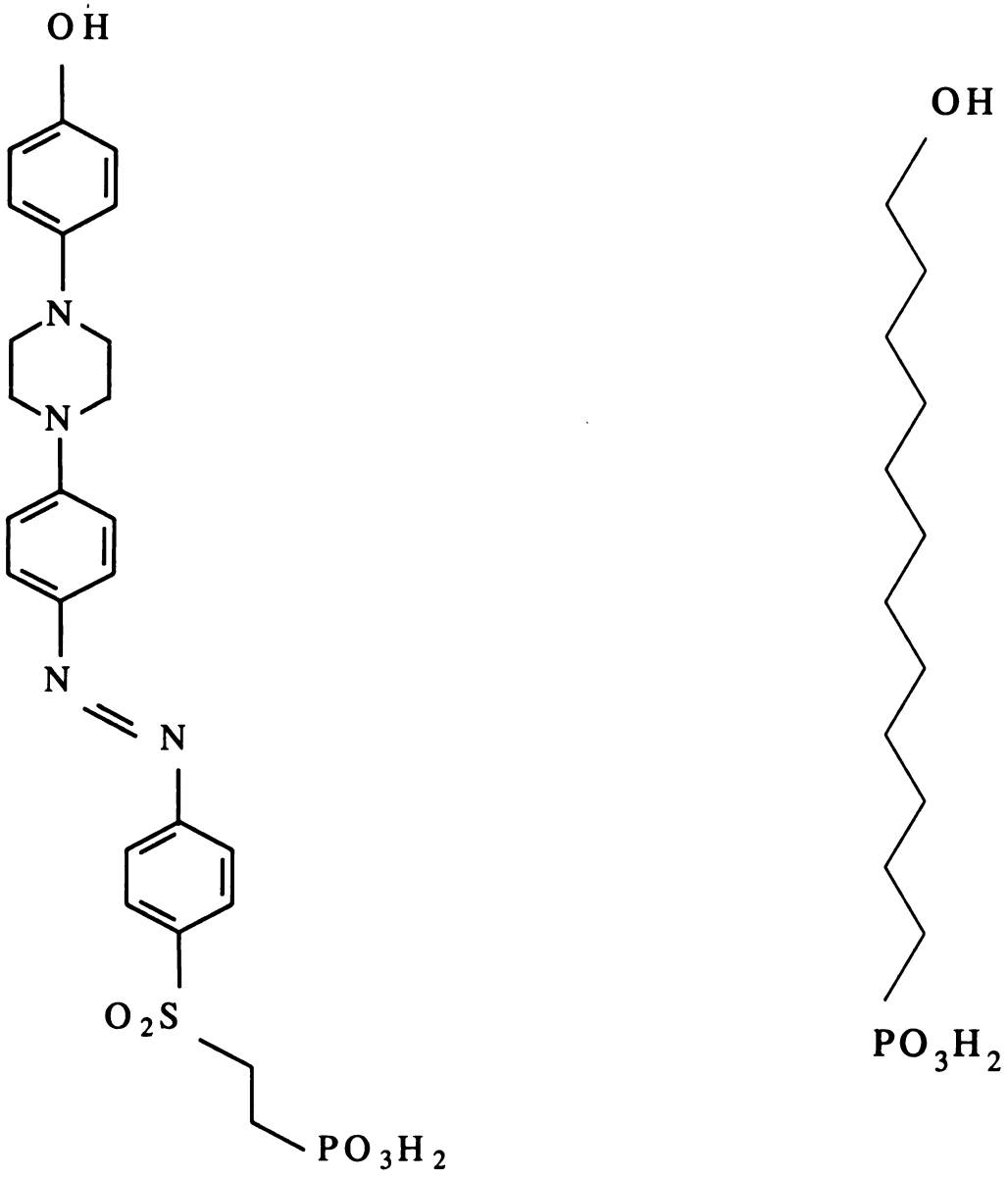

Figure 3.1: $\chi(2)$ – active chromophore (4-(4-(4-(4-((2-Hydroxyethyl) sulfonyl) phenyl) piperazinyl)-phenyl) phosphonic acid C1 and diluent molecule 1-hydroxyl-12-dodecylphosphonic acid HDPA

Figure 3.2 shows UV-Visible spectra for both solution phase C1 (top panel) and surface-bound monolayers (bottom panel). There was a slight blue-shift in the absorbance maximum of the surface-bound chromophore as its concentration in solution increased. This blue-shift was attributed to an increase in π-π interactions as the chromophore molecules are packed more closely together at higher loading density. From solution phase data the molar absorptivity, ϵ_{max}, was calculated to be 21,996 $Lmol^{-1} cm^{-1}$ for C1.[20]

To successfully study chromophore surface distribution it was essential to ensure that the solution composition, the ratio of chromophore to diluent molecule, was directly proportional to the composition of the monolayer deposited on the surface. In order to maintain the solution composition, an appropriate solvent system had to be selected; if either the chromophore or the diluent molecule were too soluble in solution the proper ratio of the two components would not be preserved on the surface. The composition of the deposition solution was determined empirically to be a 6:1:2 v/v/v ratio of acetonitrile:ethanol:dimethylformamide (DMF) with the chromophore initially contained in the DMF component. A plot of the monolayer absorbance maxima as a function of monolayer composition should maintain the same linearity, and zero y-intercept, as the solution phase measurements in order to be considered representative of the solution composition. Figure 3.3 illustrates the linear increase of absorbance with increasing chromophore concentration in solution, along with the corresponding data for the monolayer samples. The monolayer data closely follow the linear increase in absorbance of the solution phase measurements and the monolayer composition was considered to adequately represent the chromophore solution concentration on the surface.[20] Surface

loading density for monolayer adsorption was estimated using the value of ϵ_{max} determined from solution phase data and the experimental monolayer absorbance (ϵ_{max} = 21,996 $Lmol^{-1}cm^{-1}$, A_{max} = 0.031 for 100% C1). Based on these values surface loading density for C1 was estimated as 8.5 x 10^{14} $cm^{-2}layer^{-1}$.

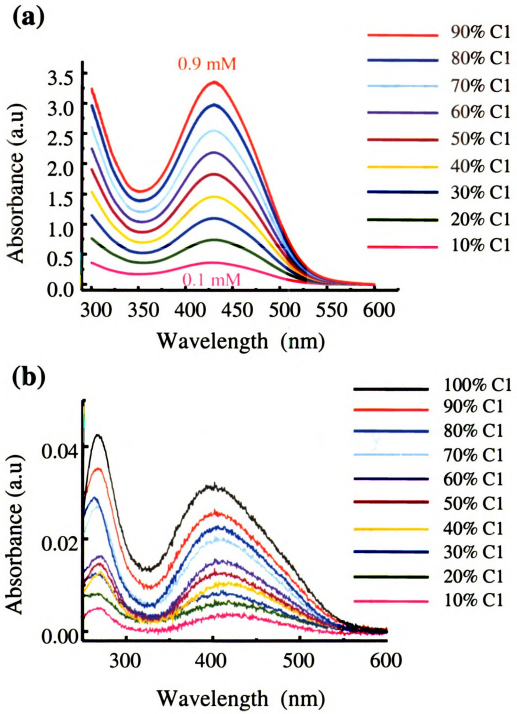

Figure 3.2: **(a)** UV-Visible data for solution phase C1.
(b) UV-Visible data for surface-bound bilayers of C1.

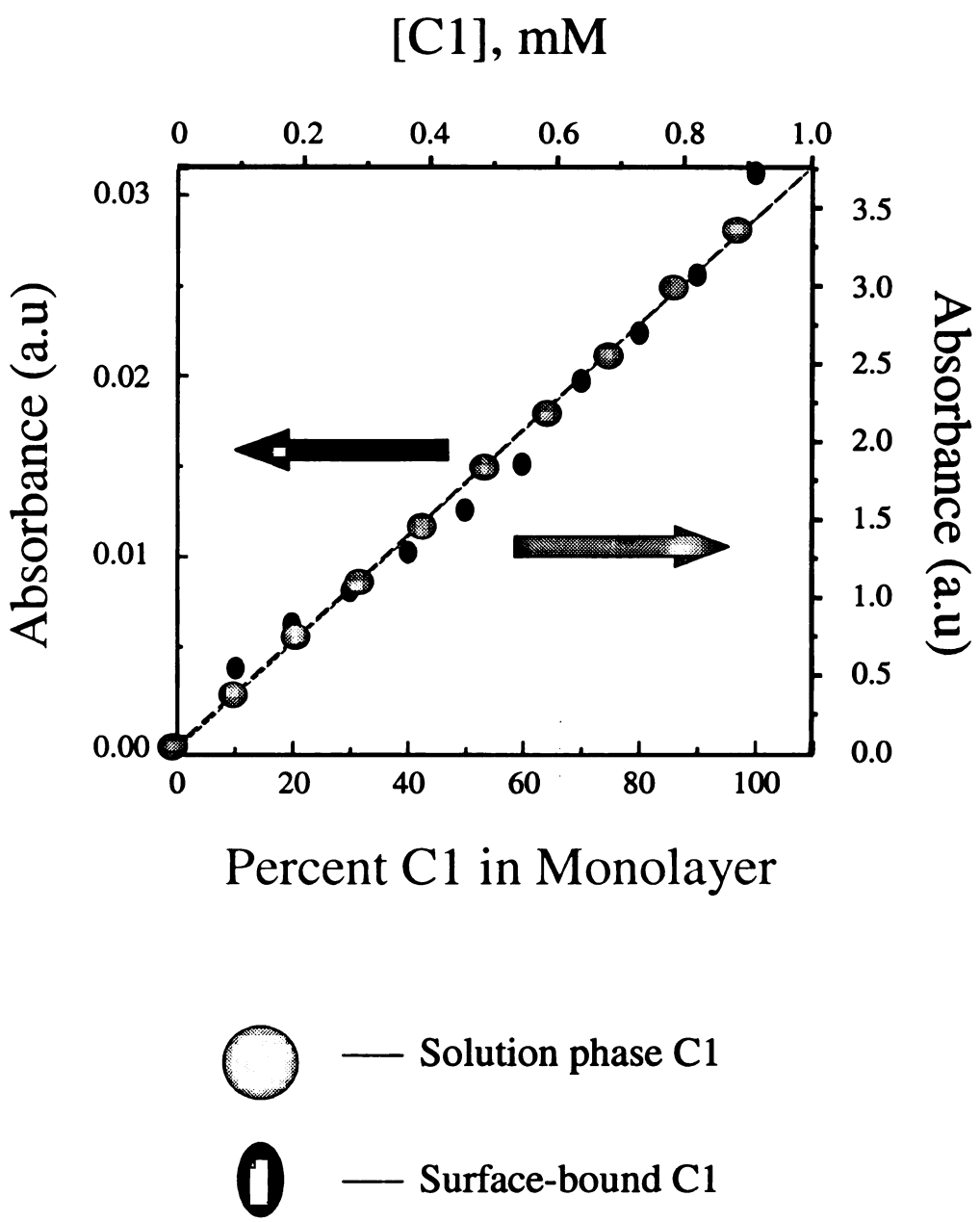

Figure 3.3: Plots of absorbance maxima vs. concentration C1 (in solution) and %C1 (in monolayer). Absorbance of surface-bound C1 increases with the same slope as solution phase C1, maintaining the ratio of chromophore to diluent in monolayer formation.

3.3 Results and Discussion

In Fig. 3.4 we show a series of selected monolayer raw images spanning 0% (blank) to 100% C1 surface coverage (see Appendix A for the full sample series). It is clear that there are distinct changes in image appearance as the concentration of the chromophore is increased. There is also substantial variation in the images from location to location *within* each sample. The first issue to consider is the appearance of "ripples" in the raw image data. One possible explanation for these features is simple optical interference between the two incident beams. If this were the case, the "ripples" should exhibit an orientational dependence that depends significantly on the input polarization, and the period of the interference pattern would be constant for a given optical configuration. The ripples should form a cross-hatched pattern upon subtraction of the 0° and 90° images if they are artifacts of optical interference. We find, however, that the "ripple" features remain, even in the difference image, and, more significantly that the period of these features varies substantially over the face of the sample within a single image, ruling out simple optical interference as the cause.

There are two other possible causes for these features. Either they are genuine spatial heterogeneity in the samples or they represent an interference pattern between second harmonic light generated at the front and back faces of the SiO_x substrate. In this picture, the spatial variations in the ripple pattern would be reflective of changes in the thickness of the quartz plates we use across the width of the irradiated region. Because of substrate thickness (~1 mm) and the angle between the incident fundamental beams, having the beams co-focused on the front face would place them ~350 μm apart on the back face. Since their focal diameters are ~110 μm each, the beams would not be

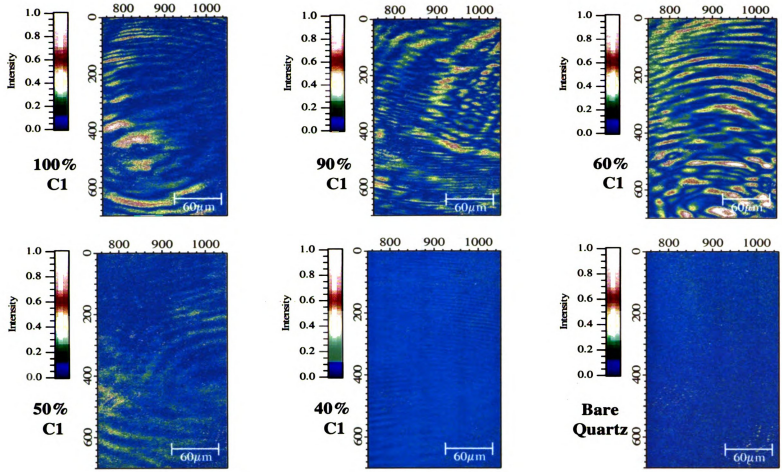

Figure 3.4: Selected raw images of C1 monolayers from 100% to 0% chromophore concentration. Note the changes in image appearance as the C1 concentration was varied. For samples with C1 concentration below 50%, the image more closely resembles that of bare quartz.

overlapped on the back face of the sample, ruling out interference between front and back face SHG signal that would be aligned with the microscope collection optics. We believe that the features seen on the surface second harmonic images, while they may contain some optical interference component, are dominated by the surface morphology of the interfaces we are examining.

Another point of consideration is any quadrupolar response arising from the quartz substrate. Guyot-Sionnest and Shen determined that the SHG from a surface was composed of an electric dipole (local contribution) term, an electric quadrupole term (nonlocal contribution), and a magnetic dipole term.[21] The electric quadrupole contribution was found to be substantial for interfaces *without* significant polar ordering of molecules in the surface layer. Electric dipole contributions were found to be dominant for interfacial layers which had significant polar ordering of the molecules and either the fundamental or second harmonic wavelength resonant with an allowed electric dipole transition.[21] Flory and Blanchard have also determined that the quadrupolar term dominates the SH signal at normal incidence for a bare silica substrate.[22] For the imaging experiments of this work the incidence angle of the fundamental beam is non-normal and the second harmonic at 532 nm is on the red edge of the absorption band of C1 (see Figure 3.2). The π-π interactions of the chromophore should also provide some measure of order within the monolayer so it is likely that dipolar contributions to the second harmonic are dominant for these experiments.

For each of the raw images we have selected 20 100 x 100 pixel areas (corresponding to 60 x 60 μm on the sample) at random and have performed autocorrelation analysis on them, using the protocol outlined in section 2.6.

The autocorrelation functions reflect the surface feature heterogeneity in the raw images. Figure 3.5 illustrates the wide variety of autocorrelation functions that can be obtained from a single sample. Regions of the AC function having normalized correlation amplitudes greater than 0.6 we consider to be areas of high correlation.

Once the autocorrelation function was obtained, a line profile through the maximum correlation intensity was extracted. We show selected autocorrelations in Figure 3.6 for monolayers containing 100%, 60%, and 30% C1. The higher chromophore loading density samples exhibit fairly large regions of high correlation across the entire 100 x 100 pixel region of interest. Samples having a chromophore loading density below 50%, however, do not exhibit large regions of high correlation and the correlation amplitude falls off rapidly with small displacements from the origin. Extracted line profiles are also shown next to the corresponding AC function. The line profiles appear to contain more than one type of lineshape, which may indicate the presence of more than one domain on the surface. By calculating the FWHM of the autocorrelation function line profiles, we can determine the average sizes of these distributions, which are reported in Table 3.1. Two domain sizes were observed from the FWHM calculations: a ~15μm domain for the broad component and a ~1μm domain for the narrow component. Samples having dual entries in the table indicate a line profile that seemed to contain more than one lineshape. A FWHM value was calculated for the narrow component and for the broad component according to the peak heights shown in Figure 3.7. The relative contribution of each domain varies with C1 concentration, and we show these contributions as a function of C1 loading in Figure 3.8(a).[20]

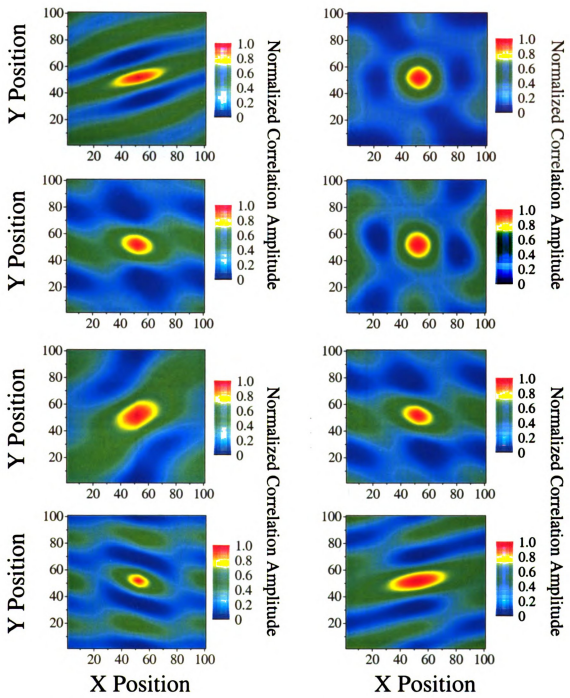

Figure 3.5: AC functions calculated for eight different randomly selected regions of a 60% C1 sample. The AC functions reflect the heterogeneity observed in the raw surface images.

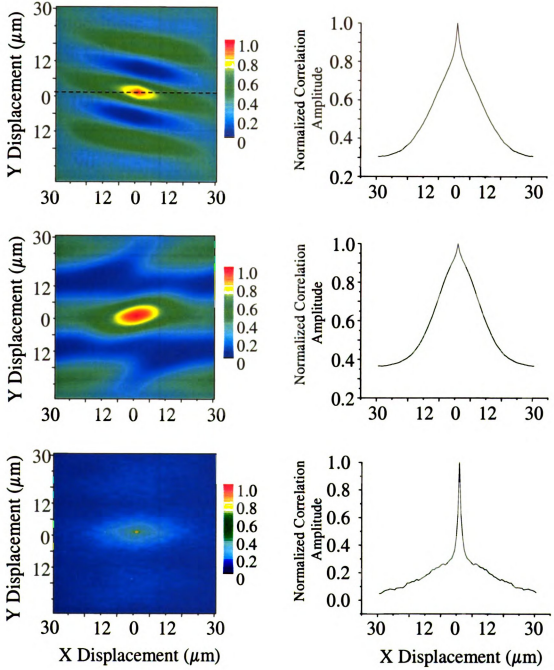

Figure 3.6: Representative AC functions for 100%, 60%, and 30% C1 (left panel) and their associated line profiles (right panel).

Monolayer Composition (% C1)	Average Feature Size (μm)	Domain Contribution (% total peak area)
100	1.0 ± 0.3	13
	17.6 ± 2.8	87
90	1.0 ± 0.3	1
	16.7 ± 3.1	99
80	0.8 ± 0.3	10
	16.8 ± 3.5	90
70	1.2 ± 0.3	11
	18.2 ± 3.4	89
60	0.8 ± 0.3	4
	15.8 ± 3.6	96
50	1.2 ± 0.3	18
	17.6 ± 4.3	82
40	0.8 ± 0.2	22
	18.5 ± 3.4	78
30	0.8 ± 0.2	17
	15.2 ± 4.6	83
20	1.0 ± 0.4	29
	17.6 ± 5.2	71
Bare Quartz	1.1 ± 0.4	-

Table 3.1: Average domain size as determined by the FWHM of extracted line profiles. Each entry is the average of 20 FWHM values. Two domain sizes appear to be present, one ~15μm domain and one ~1μm domain.

It is, of course, important to consider whether there is a physical or chemical basis for the existence of ~ 1 μm and ~ 15 μm features on a SiO_x substrate. One possible explanation is that these characteristic feature sizes are related to the manner in which the SiO_x was processed. Optical quality SiO_x is typically available in $\lambda/10$ flatness and is not polished, so these data cannot be easily accounted for in terms of polishing grooves. If there is no physical basis for the spatially heterogeneous distribution of C1 chromophores, it is possible that the features we observe are the result of spatial inhomogeneity in the distribution of surface $-OPO_3^{2-}$ groups onto which the adlayer is bound. Owing to the speed and completeness of the phosphorylation reaction, it is likely that any spatial heterogeneity in phosphate groups is reflective of a spatial variation in the distribution of reactive silanol groups. We next turn to consideration of how the surface morphological features change with the chromophore loading density. The data in Fig. 3.8 (b) bear a significant resemblance to those acquired by surface second harmonic intensity measurements for the same system (Figure 3.8 (a)).[20] This correlation is not surprising and the imaging data do provide insight into the characteristic domain sizes that is not available from SSHG intensity measurements. It is interesting to note that there is in fact some recordable persistence length for the nominally disordered domain, and that this characteristic persistence length is on the order of the wavelength of the fundamental excitation beam(s). Given the dimensional limitations of the optical imaging equipment we use and the wavelength of the fundamental electric fields, it is possible that the features characterized by a ~1 μm domain size are in fact a collection of a variety of smaller "domains" or disordered regions. Further experimentation will be required to resolve this issue.

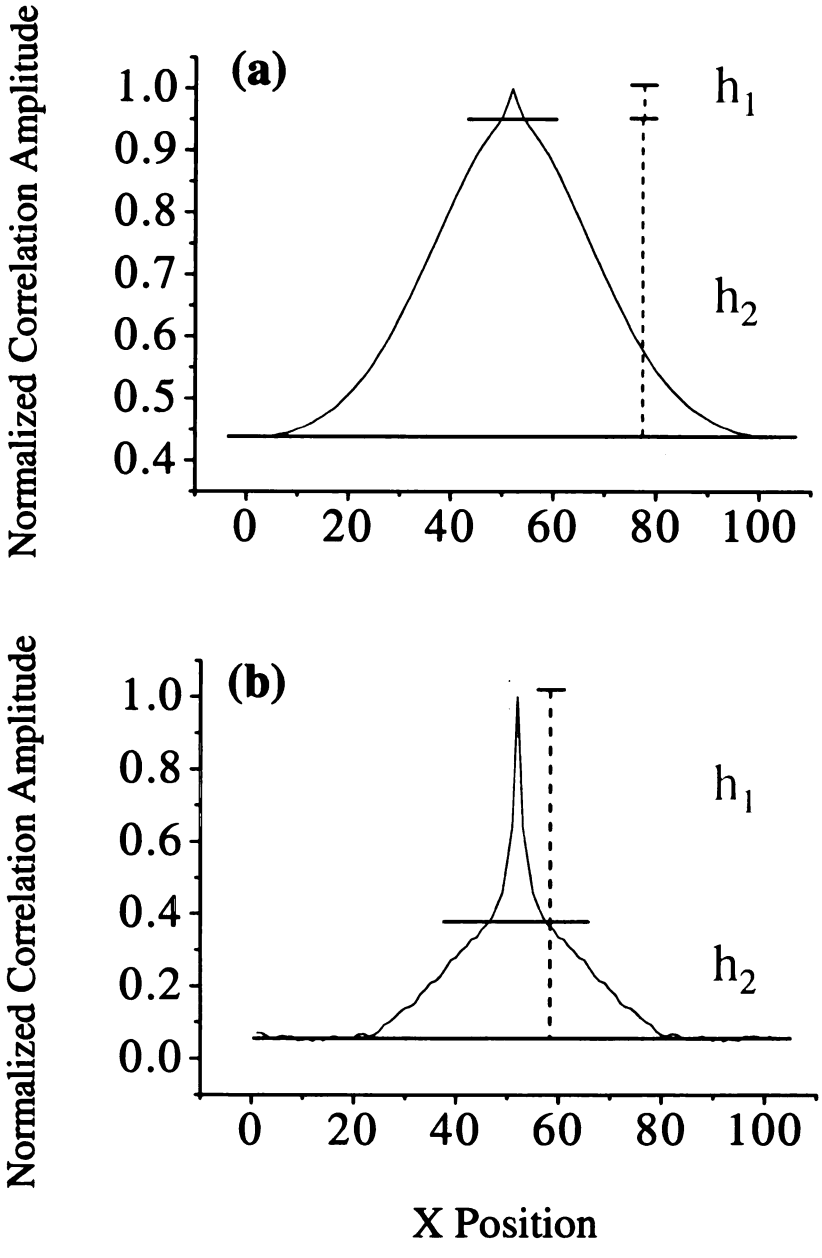

Figure 3.7: **(a)** Prevalent lineshape among higher loading density samples: ≥ 60% C1. **(b)** Prevalent lineshape among lower loading density samples: ≤ 50% C1. Two different lineshapes appear to be present in the line profiles with the lower loading density samples showing a more pronounced effect. Two FWHM values were calculated according to the peak heights indicated in the figure.

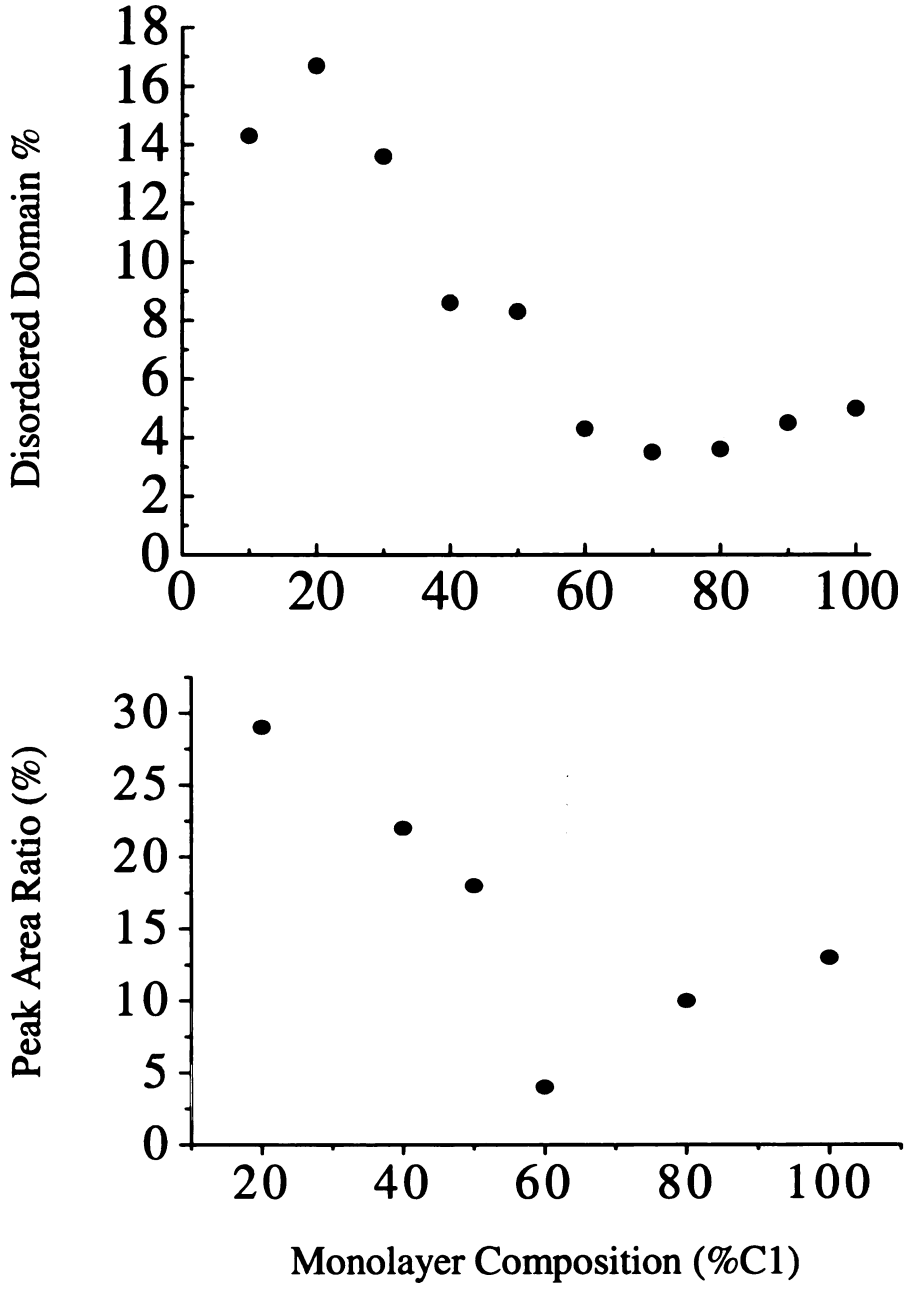

Figure 3.8: Presence of disordered domain as a function of chromophore concentration (top panel).[20] Ratio of narrow Gaussian component to total peak area as a function of chromophore concentration

3.4 Conclusions

In order to extract the persistence length of aggregation on the surface, we have developed an autocorrelation analysis protocol. This technique indicates, very clearly, changes in the relative contributions of at least two characteristic domains as a function of surface chromophore concentration. These data represent a novel means of determining characteristic length scales for systems possessing a heterogeneous distribution of surface chemical functionality. We anticipate these data to find utility in areas where silica surfaces are used, such as chemical separations and certain types of device fabrication.

Images in this thesis are presented in color and may not translate accurately to black and white

3.5 Literature Cited

1. Simpson, G.J.; *Appl. Spectrosc.*, **2001**, *55*(1), 16A.

2. Shen, Y.R.; *Annu. Rev. Phys. Chem.*, **1989**, *40*(327.

3. Corn, R.M. and Higgins, D.A.; *Chem. Rev.*, **1994**, *94*(1), 107.

4. Moreaux, L., Sandre, O., and Mertz, J.; *Journal of the Optical Society of America B: Optical Physics*, **2000**, *17*(10), 1685.

5. Campagnola, P.J., Wei, M.-D., Lewis, A., and Loew, L.M.; *Biophys. J.*, **1999**, *77*(6), 3341.

6. Schaller, R.D., Roth, C., Raulet, D.H., and Saykally, R.J.; *J. Phys. Chem. B*, **2000**, *104*(22), 5217.

7. Schaller, R.D., Johnson, J.C., and Saykally, R.J.; *Anal. Chem.*, **2000**, *72*(21), 5361.

8. Floersheimer, M., Paschotta, R., Kubitschek, U., Brillert, C., Hofmann, D., Heuer, L., Schreiber, G., Verbeck, C., Sohler, W., and Fuchs, H.; *Appl. Phys. B: Lasers and Optics*, **1998**, *B67*(5), 593.

9. Rosenfeldt, A. and Florsheimer, M.; *Applied Physics B: Lasers and Optics*, **2001**, *73*(5-6), 523.

10. Mishina, E.D., Sherstyuk, N.E., Vorotilov, K.A., Sigov, A.S., Barberi, R., Moret, M.P., Manders, F., De Santo, M.P., Larsen, P.K., and Rasing, T.; *Appl. Phys. B: Lasers and Optics*, **2002**, *74*(7-8), 783.

11. Smolyaninov, I.I., Liang, H.Y., Lee, C.H., and Davis, C.C.; *J. Appl. Phys.*, **2001**, *89*(1), 206.

12. Beermann, J., Bozhevolnyi, S.I., Pedersen, K., and Fage-Pedersen, J.; *Opt. Commun.*, **2003**, *221*(4-6), 295.

13. Florsheimer, M., Jundt, D.H., Looser, H., Sutter, K., Kuepfer, M., and Guenter, P.; *Ber. Bunsen-Ges. Phys. Chem.*, **1994**, *98*(3), 521.

14. Florsheimer, M., Bosch, M., Brillert, C., Wierschem, M., and Fuchs, H.; *J. Vac. Sci. Technol., B*, **1997**, *15*(4), 1564.

15. Neuberth, U., Walter, L., von Freymann, G., Schimmel, T., Wegener, M., Khitrova, G., and Gibbs, H.M.; *Appl. Phys. Lett.* , **2002**, *81*(10), 1881.

16. Wiseman, P.W. and Petersen, N.O.; *Biophys. J.*, **1999**, *76*(2), 963.

17. Goldbeck-Wood, G., Bliznyuk, V.N., Burlakov, V., Assender, H.E., Briggs, G.A.D., Tsukahara, Y., Anderson, K.L., and Windle, A.H.; *Macromolecules*, **2002**, *35*(13), 5283.

18. Bischoff, M.M.J., Yamada, T.K., and van Kempen, H.; *Physical Review B: Condensed Matter and Materials Physics*, **2003**, *67*(16), 165403/1.

19. Katz, H.E., Wilson, W.L., and Scheller, G.; *J. Am. Chem. Soc.*, **1994**, *116*(15), 6636.

20. Bakiamoh, S.B. and Blanchard, G.J.; *Langmuir*, **2002**, *18*(16), 6246.

21. Guyot-Sionnest, P. and Shen, Y.R.; *Physical Review B: Condensed Matter and Materials Physics*, **1987**, *35*(9), 4420.

22. Flory, W.C., Mehrens, S.M., and Blanchard, G.J.; *J. Am. Chem. Soc.*, **2000**, *122*(33), 7976.

Chapter 4

SURFACE DISTRIBUTION OF NONLINEAR OPTICAL CHROMOPHORES IN MULTILAYER ASSEMBLIES

SUMMARY

We report on the imaging of multilayer assemblies of the nonlinear chromophores (4-(4-(4-(4-((2-hydroxyethyl) sulfonyl) phenyl) piperazinyl)-phenyl) phosphonic acid **(C1)** and (2-(4-(4-(4-(4-hydroxyphenyl)piperazinyl)phenyl)azophenyl)sulfonyl)ethyl-phosphonic acid **(C2)**. The C1 multilayer assembly exhibited atypical layer growth between layers two and three, which may indicate a change in morphology for this system. A decrease in correlation upon additional layer deposition was also observed for the C1 sample with calculated feature sizes dropping slightly from ~14 to ~7μm. The C2 multilayer assembly produced an average feature size of ~10 μm, however, exhibited no decreasing trend in feature size with the number of deposited layers.

4.1 Introduction

Numerous reports in the literature show that second harmonic generation is a useful technique for studying a wide variety of monolayer systems at different types of interfaces. The application of SHG to *multilayer* assemblies has been somewhat more limited due to the difficulty in maintaining well ordered, non-centrosymmetric structures over multiple layers. Marks and co-workers first reported the preparation of regular, nonlinear optically (NLO)-active multilayer structures using siloxane chemistry for self-assembly. Layer deposition consisted of three main steps: silane priming of the substrate, chromophore attachment of either a stilbazole or azo-based moiety, and deposition of a polymeric layer to improve lateral film stability and renew the hydroxylated surface for further reactive chemistry.[1, 2]

In addition to the use of siloxane chemistry, ordered multilayer assemblies based on zirconium phosphate/phosphonate layer growth have also been successfully demonstrated.[3-7] In an effort to better understand the morphology of organophosphonate deposition, Thompson et al. performed a series of atomic force microscopy (AFM) experiments.[8] The adsorption of hexadecane bisphosphonic acid (C_{16}BPA) on a zirconium (IV)-rich surface was monitored by AFM for sample incubation times of 20, 110, and 200 minutes. Prior to the addition of the C_{16}BPA, AFM imaging showed a uniformly zirconated surface with very little of the exposed silicon substrate visible. After 20 and 100 minute incubation times AFM images clearly showed island features where C_{16}BPA had adsorbed. While Thompson and co-workers did not comment on the lateral size of the island features, by inspection of the AFM images they range from 25nm to >100nm. AFM images of the 200 min incubation time showed uniform surface

coverage of C_{16}BPA, similar to the zirconated surface. Interestingly, although initial adsorption of the C_{16}BPA film occurs as island-like structures, with long enough incubation times the bare areas of the substrate fill in until the monolayer is uniform.

The experiments of Thompson and co-workers discussed previously also included the AFM imaging of a C_{16}BPA bilayer. Deposition times were chosen so that incomplete layer formation would occur for each layer of C_{16}BPA. Three regions were apparent in the AFM image of the bilayer: monolayer coverage, bilayer coverage, and the zirconated surface. Bilayer formation, however, did not occur uniformly on the surface, so that large areas of only monolayer coverage were still visible.[8]

The AFM image of the bilayer assembly discussed above was taken after deposition of the second C_{16}BPA layer. Therefore, it cannot be said definitively whether bare patches of zirconated substrate would fill in with C_{16}BPA upon deposition of the second layer. From the results of Thompson's monolayer experiments, however, it is reasonable to expect that multilayer films are also capable of 'self-healing.' Hence, with the deposition of subsequent layers, adsorbate may fill in unoccupied portions of the substrate (or incomplete under-layers) until the film is uniform.

Second harmonic microscopy applied to the imaging of interfacial systems is growing to be a useful and nondestructive tool for the in situ analysis of many systems. While LB films and covalently bound monolayers have been imaged successfully, to date the SH imaging of multilayer structures has not been attempted. Successful SH imaging would lead to elucidating information about the changes in feature size (if any) in multilayer films upon multiple adlayer deposition processes.

4.2 Experimental

Figure 4.1 shows the structures of C1 and C2. The nonlinear chromophore C1 has been reported previously by Katz et. al. and the chromophore C2 has been synthesized previously in our group by Flory and Bakiamoh.[4, 7, 9] Multilayer assemblies of 5 bilayers (both faces of a quartz slide = one bilayer) of each chromophore were prepared with the following method.

Multilayer samples were prepared for surface image acquisition by using zirconium phosphate/phosphonate linking chemistry. A quartz substrate was cleaned in piranha solution (3:1 sulfuric acid:hydrogen peroxide, ***caution: strong oxidizer!!!)*** for 15 minutes, rinsed with distilled water, and dried under nitrogen. The sample was then activated, under inert atmosphere, in a solution of anhydrous acetonitrile, 2,4,6-collidine (0.3M), and phosphorous oxychloride (0.3M). Immersion time for the surface activation was 30 minutes, after which the sample was rinsed with reagent grade acetonitrile, distilled water, and dried under nitrogen. Following phosphorylation, the substrate was immersed in a 10mM solution of $ZrOCl_2$ (in 60:40 ethanol:water v/v) for 15 minutes, then rinsed with distilled water and dried with nitrogen. Once zirconation was complete the sample was immersed in the appropriate 0.5mM chromophore solution and heated to ~50° C for 1 hour.

After substrate exposure to the chromophore, the layer was characterized using UV-Visible spectrometry (Varian Cary Bio300) and optical null ellipsometry (Rudolph Auto EL) to ensure that chromophore adsorption had occurred. Once adlayer presence was verified the sample was mounted in the second harmonic microscopy instrument and surface images were acquired for three separate spots on the sample face. All images

were acquired with a 10 minute acquisition time and a camera temperature of -98.5°C. Images were acquired at 0° and 90° polarization rotation of the fundamental and all polarizations of the second harmonic were collected.

After surface image acquisition for the newly formed layer was complete, the surface was re-activated and another chromophore layer deposited by the procedure described above. This cycle of layer deposition followed by surface imaging was repeated until 5 bilayers for each chromophore were imaged. Surface image analysis was performed on difference images, according to the protocol outlined in section 2.6.

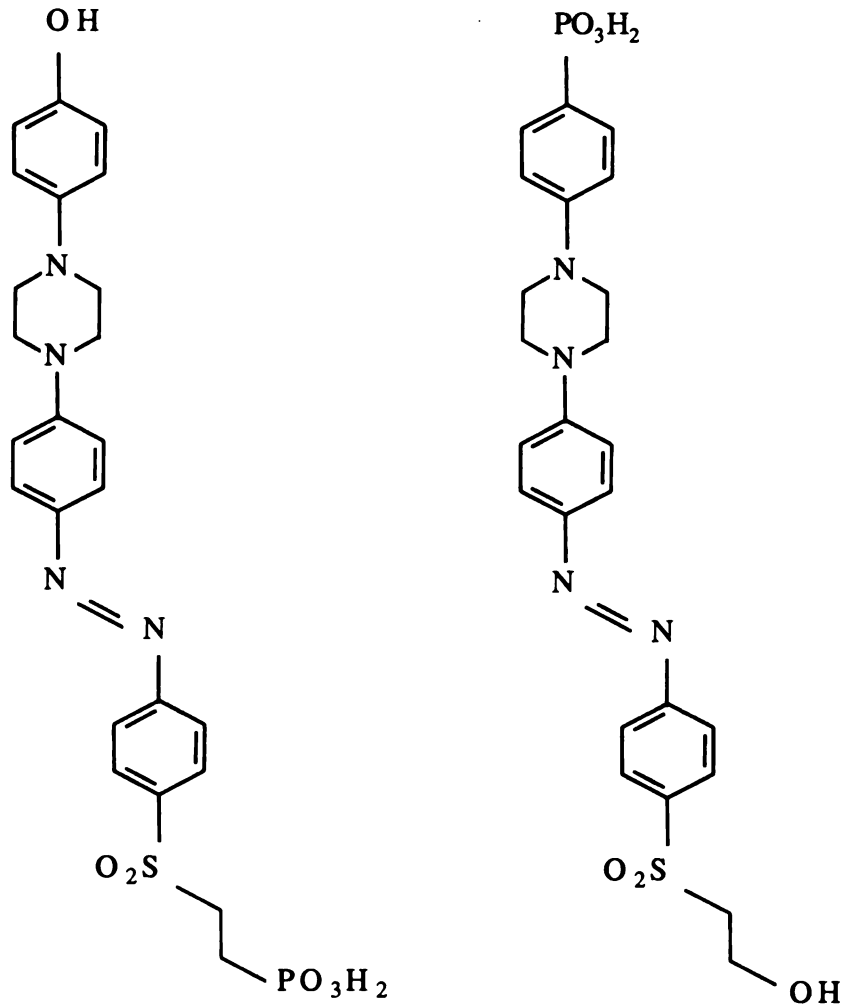

C1 **C2**

Figure 4.1: $\chi(2)$ – active chromophores (4-(4-(4-(4-((2-Hydroxyethyl) sulfonyl) phenyl) piperazinyl)-phenyl) phosphonic acid **(C1)** and (2-(4-(4-(4-(4-hydroxyphenyl)piperazinyl)phenyl)azophenyl)sulfonyl) ethylphosphonic acid **(C2)**.[4,7]

4.3 Results and Discussion

We were interested in determining whether the surface distribution of a nonlinear chromophore changes in a regular way upon increasing the number of layers adsorbed onto the surface. In order to study this we have constructed two, five bilayer assemblies of two nonlinear chromophores, C1 and C2. First we consider the UV-Visible and ellipsometric data and then discuss the imaging of the C1 and C2 assemblies.

The absorbance, as a function of deposited layers, did not increase linearly for the C1 sample and will be discussed presently. Figure 4.2 shows the UV-Visible data for the 5 bilayer assemblies of C1 and C2. For chromophore one, there is almost no difference in the visible absorbance band for layers two and three, however, the UV-band still shows increasing absorbance. Increasing absorbance in the UV-band and not in the visible-band may indicate some sort of morphology change in the film upon adsorption of layer 3; however, linear absorbance increases with increasing number of layers for ZP films has been well documented.[8, 10-12] The lack of increase in the visible absorption band between layers two and three is more likely due to poor surface activation of layer two by phosphorous oxychloride. Ellipsometric data show fairly regular layer growth for C1 (Figure 4.3a), however, ellipsometry was performed on polished silicon substrates. While the mechanism of layer growth is assumed to be the same on either quartz or silicon substrates, it is possible to have an inadequate activation step on one sample and not the other. Even allowing for the poor adsorption of layer three, information concerning the other four layers of the C1 multilayer assembly was analyzed.

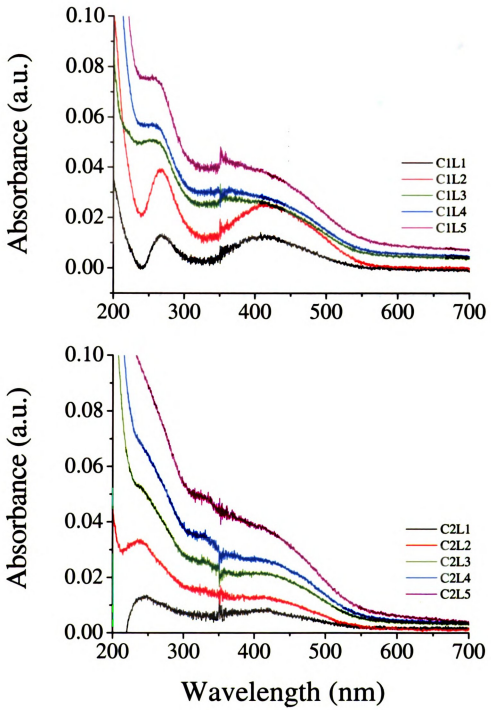

Figure 4.2: UV-visible data for multilayer samples of C1 (top) and C2 (bottom). Note that layer 3 for the C1 sample does not exhibit linear loading density.

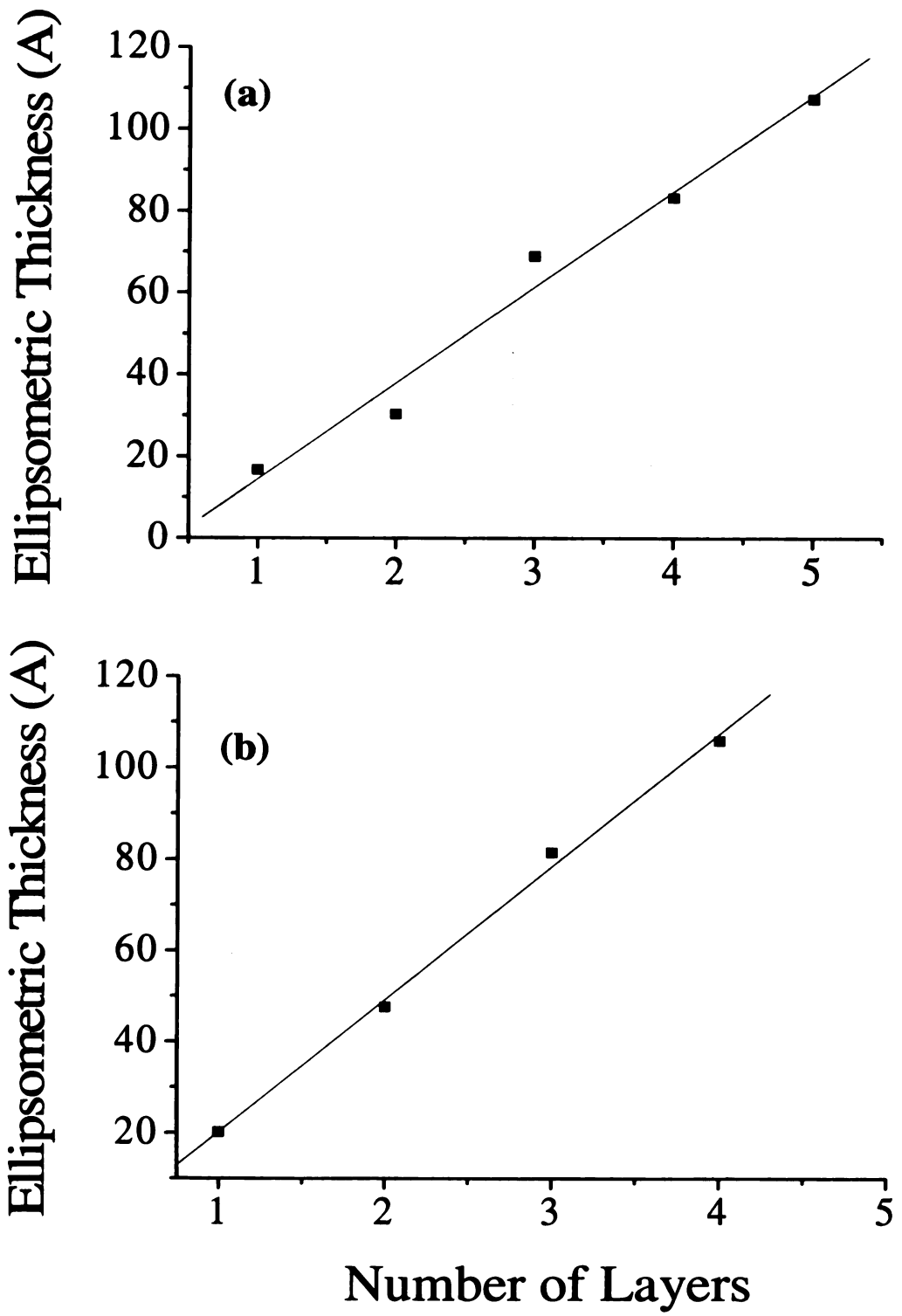

Figure 4.3: Ellipsometric data for 5 bilayer assemblies of C1 **(a)** and C2 **(b)**.

Aucocorrelation Function Analysis

It has been shown that the adsorption of zirconium phosphate/phosphonate films initially occurs as island structures.[8] For monolayer systems it has also been shown that with a long enough incubation time the bare patches between the islands fill in to form a uniform layer. But does this process occur with multilayer films as well? If the island structures are distributed randomly then there should be no correlation exhibited in the AC function away from the origin. Upon initial layer deposition, assuming the formation of islands, one might expect moderate correlation over the region of interest mixed with patches of zero correlation possibly representing bare patches of substrate. Since silica is an amorphous substrate, the active silanol groups are randomly distributed and would not be correlated in any way. Once chromophore is present, however, van der Waals interactions between chromophore molecules may produce some degree of structural order on the surface. If the underlayers do indeed begin to fill in upon deposition of additional layers then one might expect the patches of zero correlation to diminish in the AC function and regions of low to moderate correlation increase. In this section we will first discuss a simulated image of random intensities and its resulting autocorrelation function followed by the results obtained from the C1 and C2 multilayer assemblies.

As stated previously, a surface with randomly distributed island structures should show no correlation in the AC function away from the origin. Figure 4.4 is a randomly generated image using OriginPro 7.0 software. A 100 x 100 matrix was filled with uniform random numbers, meaning a random number between zero and one was assigned to each cell of the array. The exported text file was then processed in Mathematica according to the procedure outlined in chapter 2.6.

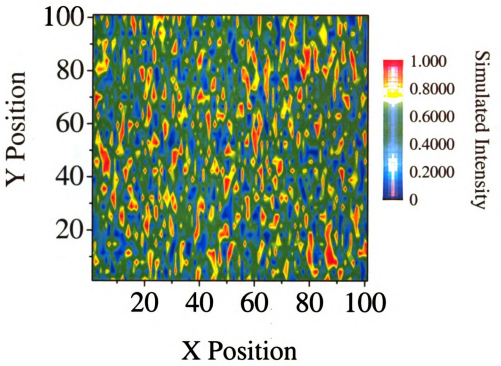

Figure 4.4: A simulated image of randomly distributed intensities.

The autocorrelation function generated from the random image shown in Figure 4.4 is illustrated in Figure 4.5(a). Note that there is no correlation at all away from the origin. Figure 4.5(b) is the enlarged region enclosed by the white border in 4.5(a). As seen from the enlargement of the AC function, displacements of more than one pixel result in a total loss of any correlation. To further illustrate the sharp fall off of the normalized correlation amplitude, a line profile through the origin is shown in 4.5(c). The line profile has a FWHM of one pixel as expected from inspection of the enlargement of the AC function.

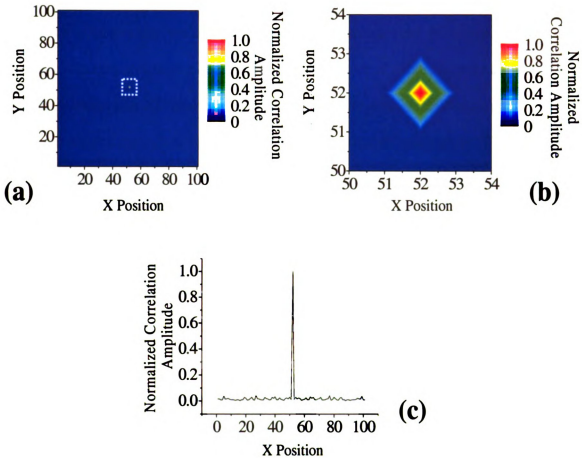

Figure 4.5: **(a)** Calculated autocorrelation function for the simulated image of Figure 4.4. **(b)** Enlargement of the region surrounding the origin the AC function of (a). Note that all correlation falls off at displacements of more than one pixel from the origin. **(c)** Line profile through the origin of the AC function in (a).

Now we turn to a discussion of the results obtained for the C1 multilayer assembly. Figure 4.6 shows selected autocorrelation functions for layers one through five. A complete set of calculated autocorrelation functions can be found in Appendix B. Layers one and two show the largest regions of correlation around the origin and as more layers are adsorbed this region begins to diminish in favor of a more loosely correlated surface. For example, AC functions of layers four and five have relatively small correlated regions around the origin; however, they exhibit diffuse regions of correlation (~0.2 normalized correlation amplitude) over most of the region of interest. Therefore, as additional layers are deposited on the surface, regions are less likely to be related to each other in a significant way. Layer three exhibits a different AC function than either layers one and two or layers four and five. Recall from the UV-Visible data presented earlier there was anomalous behavior concerning the deposition of layer three in this assembly. The AC function of layer three may represent a transition from the large, correlated regions of layers one and two to the more diffuse AC functions of layers four and five.

In the context of deposition occurring initially as islands, it is reasonable for layers one and two to show the highest degree of correlation; since the islands would provide a more ordered surface than the silanol groups of the silica substrate. The large patches of zero correlation in these AC functions may be the result of bare patches of substrate or regions where adsorption did not take place. For layer deposition to continue the molecules comprising the island structures must be activated so that a potentially smaller area is available for adsorption of the next layer. Many small islands are less likely to be related to one another since they begin to resemble a randomized surface.

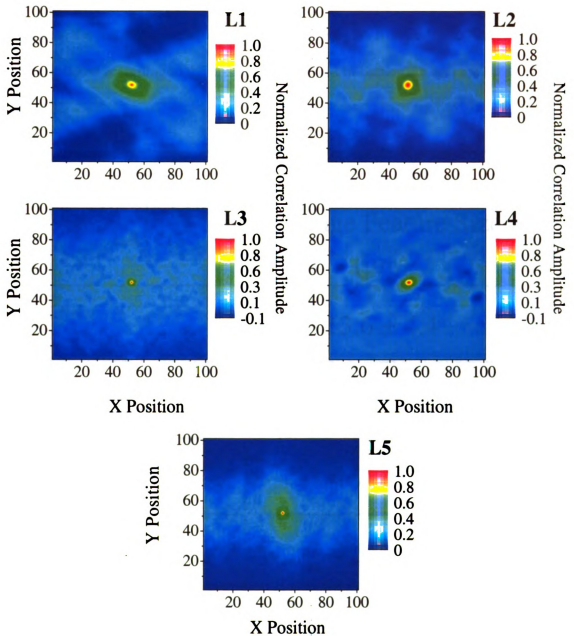

Figure 4.6: Select AC functions for the C1 multilayer assembly. A decrease in correlation is observed with increasing number of layers.

The reduction in correlation of the AC functions of layers four and five is likely indicative of the presence of many small island structures on the surface. To further investigate the reduction in correlation exhibited by layers four and five, FWHM values were calculated according to the procedure described in section 2.6 and are listed in Table 4.1.

Number of Layers	C1 Assembly Average Feature Size (μm)
1	13.6 ± 4.4
2	15.8 ± 7.9
3	4.7 ± 1.0
4	9.5 ± 3.2
5	5.3 ± 2.3

Table 4.1: Average feature sizes calculated for the C1 multilayer assembly

Layers four and five do exhibit smaller average feature sizes than layers one and two, though within the experimental error they are quite close. It is also interesting to note that the feature sizes observed here are comparable to the large domain observed for the monolayer experiments (~15μm). Even for the smaller domain sizes observed for layers four and five the average feature size is still larger than the spatial resolution limit of the camera (2μm for the 10x objective), and are therefore considered independent features, not artifacts from resolution limitations.

Since the C2 molecule is identical to C1, with only the termini exchanged, AC functions similar to those obtained for the C1 sample are expected for the C2 assembly. Figure 4.7 shows selected autocorrelation functions for the C2 sample. Unlike the C1 assembly, layers four and five in the C2 sample exhibit comparable correlation to layers one and two. For the AC functions shown in Figure 4.7, layer four shows particularly strong correlation in the x-direction across the entire region of interest. Since the substrates were not polished prior to use, such strong correlation at layer four may correspond to a groove or perhaps a scratch on the surface where adsorption was particularly favorable. Table 4.2 shows the average feature sizes calculated for the C2 multilayer assembly as a function of deposited layers. Layer two had a much lower feature size than expected considering the results obtained for the C1 sample and the similarity of the chromophores. The entire set of AC functions calculated for layer 1 showed low to moderate correlation over most of the region of interest (see Appendix B). It is possible that small enough island structures were achieved after the second deposition step to significantly impact the AC functions for layer 2.

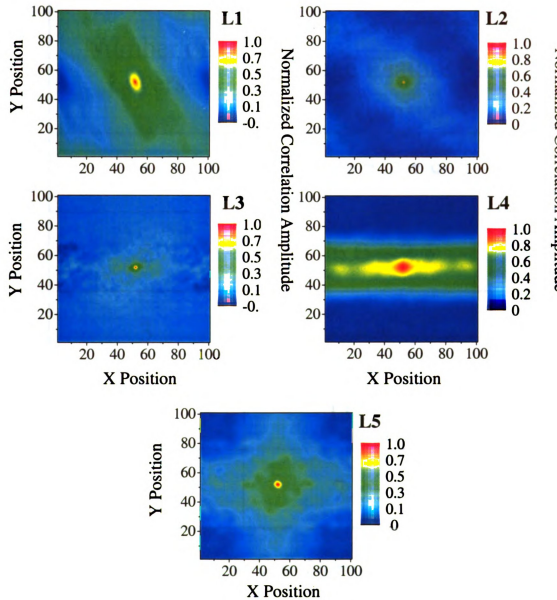

Figure 4.7: Select AC functions for the C2 multilayer assembly. Unlike the C1 sample, no decrease in correlation is observed with increasing number of layers.

Number of Layers	C2 Assembly Average Feature Size (μm)
1	13.7 ± 7.8
2	6.0 ± 2.5
3	4.8 ± 2.0
4	11.5 ± 7.4
5	7.8 ± 4.6

Table 4.2: Average feature sizes for multilayer samples of C2.

The trend toward decreasing feature size with increasing number of layers observed for the C1 sample is not present here and the calculated FWHM value for layer four is comparable to that of layer one. The calculated feature sizes, however, are still comparable to the large domain size observed in the monolayer experiments.

4.4 Conclusions

We have fabricated two multilayer assemblies of the nonlinear chromophores (4-(4-(4-(4-((2-Hydroxyethyl) sulfonyl) phenyl) piperazinyl)-phenyl) phosphonic acid **(C1)** and (2-(4-(4-(4-(4-hydroxyphenyl)piperazinyl)phenyl)azophenyl)sulfonyl) ethylphosphonic acid **(C2)**. The C1 multilayer assembly exhibits a decreasing degree of correlation as the number of deposited layers increases. In the context of island like deposition of ZP films this result is reasonable since small islands are less likely to be correlated and begin to resemble a randomized surface. Average feature sizes calculated for the C1 sample were ~11μm, in reasonable agreement with the larger feature size observed in the monolayer experiments of chapter three (~15μm). The C2 multilayer assembly produced more uniform feature sizes per layer with an average of ~10μm, also in fair agreement with the monolayer results.

Images in this thesis are presented in color and may not translate accurately to black and white

4.5 Literature Cited

1. Li, D., Ratner, M.A., Marks, T.J., Zhang, C., Yang, J., and Wong, G.K.; *J. Am. Chem. Soc.*, **1990**, *112*(20), 7389.

2. Lin, W., Lin, W., Wong, G.K., and Marks, T.J.; *J. Am. Chem. Soc.*, **1996**, *118*(34), 8034.

3. Katz, H.E., Scheller, G., Putvinski, T.M., Schilling, M.L., Wilson, W.L., and Chidsey, C.E.D.; *Science (Washington, DC, United States)*, **1991**, *254*(5037), 1485.

4. Katz, H.E., Wilson, W.L., and Scheller, G.; *J. Am. Chem. Soc.*, **1994**, *116*(15), 6636.

5. Neff, G.A., Helfrich, M.R., Clifton, M.C., and Page, C.J.; *Chem. Mater.*, **2000**, *12*(8), 2363.

6. Bakiamoh, S.B. and Blanchard, G.J.; *Langmuir*, **2001**, *17*(11), 3438.

7. Flory, W.C., Mehrens, S.M., and Blanchard, G.J.; *J. Am. Chem. Soc.*, **2000**, *122*(33), 7976.

8. Byrd, H., Snover, J.L., and Thompson, M.E.; *Langmuir*, **1995**, *11*(11), 4449.

9. Bakiamoh, S.B. and Blanchard, G.J.; *Langmuir*, **2002**, *18*(16), 6246.

10. Lee, H., Kepley, L.J., Hong, H.G., Akhter, S., and Mallouk, T.E.; *J. Phys. Chem.*, **1988**, *92*(9), 2597.

11. Fang, M., Kaschak, D.M., Sutorik, A.C., and Mallouk, T.E.; *J. Am. Chem. Soc.*, **1997**, *119*(50), 12184.

12. Vermeulen, L.A., Snover, J.L., Sapochak, L.S., and Thompson, M.E.; *J. Am. Chem. Soc.*, **1993**, *115*(25), 11767.

Chapter 5

CONCLUSIONS AND FUTURE WORK

5.1 Conclusions

The body of this work demonstrates the construction and practical use of a second harmonic microscopy instrument with diffraction-limited resolution (~0.6μm for 100x). Features (bright spots) observed in the raw images obtained from the instrument were attributed to second harmonic signal from the $\chi^{(2)}$-active chromophore and not simply to electric field interference. Simple optical interference would produce a diffraction pattern with constant amplitude, periodicity, and orientation that would appear in every raw image. The periodicity of the features observed in the raw images, however, varied widely from both sample to sample and within different regions of the same sample. The images analyzed were also difference images so that the observed features were independent of polarization rotation. If the image features were due strictly to interference they would be largely removed upon subtraction of the 90° (polarization rotation) micrograph from the 0° (polarization rotation) micrograph. Therefore, optical interference was ruled out as the source of observed feature in the raw surface image.

Also described in this work is the development and implementation of an autocorrelation-based analysis protocol for the extraction of characteristic domain sizes from the raw images. Monolayer experiments indicated the presence of two characteristic domain sizes; one of ~15μm and the other ~1μm.

We have also fabricated two multilayer assemblies of the nonlinear chromophores (4-(4-(4-(4-((2-Hydroxyethyl) sulfonyl) phenyl) piperazinyl)-phenyl) phosphonic acid **(C1)** and (2-(4-(4-(4-(4-hydroxyphenyl)piperazinyl)phenyl)azophenyl)sulfonyl) ethylphosphonic acid **(C2)**. The C1 multilayer assembly exhibited a decreasing degree of correlation as the number of deposited layers increases. In the context of island-like deposition of ZP films, this result is reasonable since small islands are less likely to be correlated and begin to resemble a randomized surface. Average feature sizes calculated for the C1 sample were ~11μm, in reasonable agreement with the larger feature size observed in the monolayer experiments of chapter three (~15μm). The C2 multilayer assembly produced more uniform feature sizes per layer with an average of ~10μm, also in fair agreement with the monolayer results.

5.2 Future Directions

Future work on this project could include experiments using different beam geometries and commercially available chromophores. Figure 5.1 shows two such chromophores, disperse red 1 (DR1) and disperse orange 3 (DO3). These molecules may be covalently attached to the surface through formation of ester (or urethane) and amide (or urea) bonds respectively, depending on the activating agent. Commercial availability precludes the need for complex organic synthesis and DR1 should also show some resonant enhancement since it has a broad absorption band centered on 502nm.

To better understand chromophore surface coverage on an amorphous substrate, experiments using a collinear beam geometry could be performed. Although spatial

filtering of the second harmonic would be lost, a spectral filter inserted into the optics train after the sample would remove any residual fundamental IR. Using normal incidence would also eliminate any possible electric field interference arising from the crossed beam geometry and, since the sample would not be rotated, there would be no etalon effect from the substrate. Another useful experimental geometry would be reflection mode so that monolayers grown on silicon substrates could be studied. A polished silicon substrate would introduce a more ordered surface for imaging and may improve raw image interpretation.

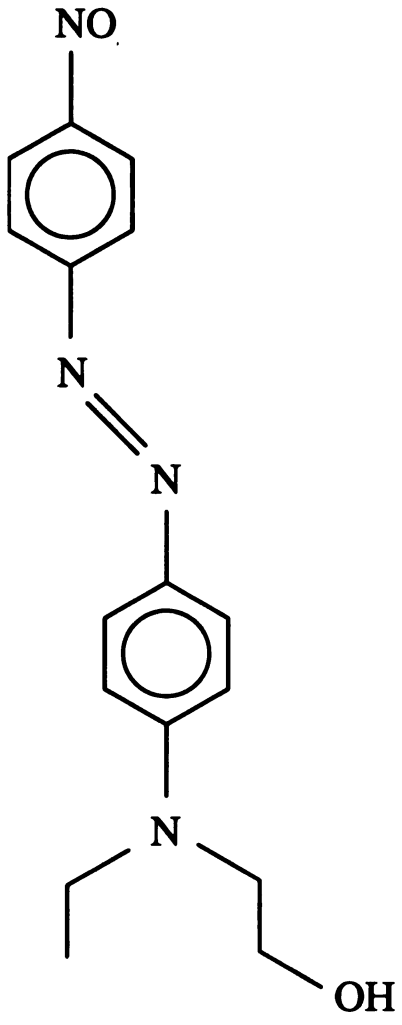

(a)
Disperse Red 1
(DR1)

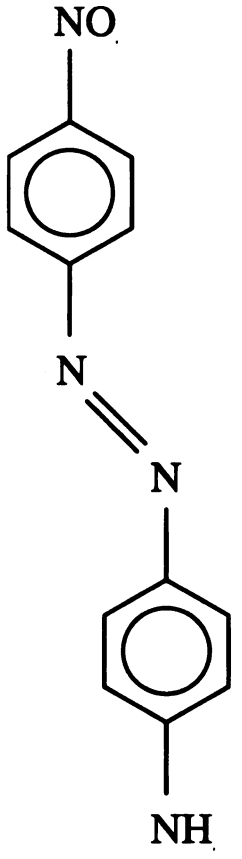

(b)
Disperse Orange 3
(DO3)

Figure 5.1: Commercially available NLO compounds **a)** disperse red 1 (DR1) and **b)** disperse orange 3 (DO3)

APPENDICES

APPENDIX A

MONOLAYER RAW IMAGE DATA: C1 DIFFERENCE IMAGES

Contained in this appendix are the raw difference images acquired for monolayers of chromophore 1. Image intensities have been normalized and all images have a false-color overlay. Monolayers range from 100% chromophore composition to 0% chromophore composition (bare quartz). The graph axes of the raw images correspond to pixel position.

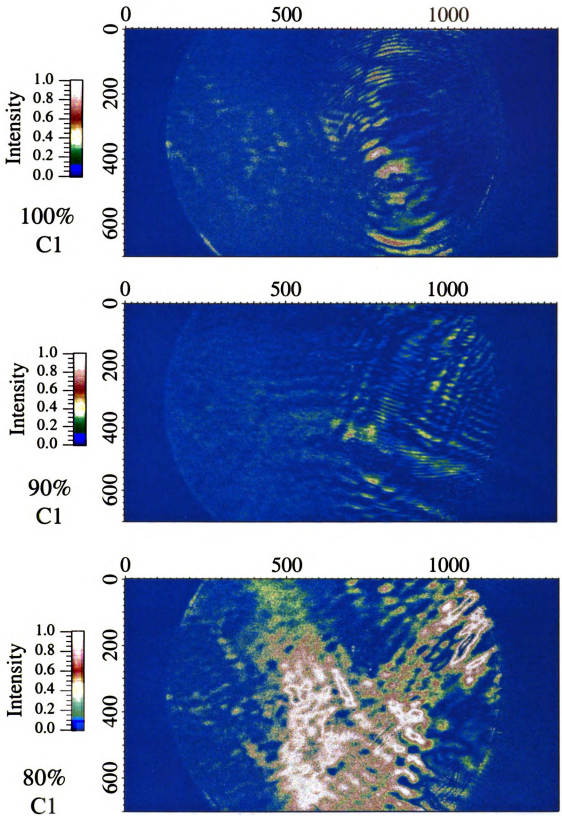
0
500
1000
0
200
400
600
Intensity
1.0
0.8
0.6
0.4
0.2
0.0
100%
C1
90%
C1
80%
C1

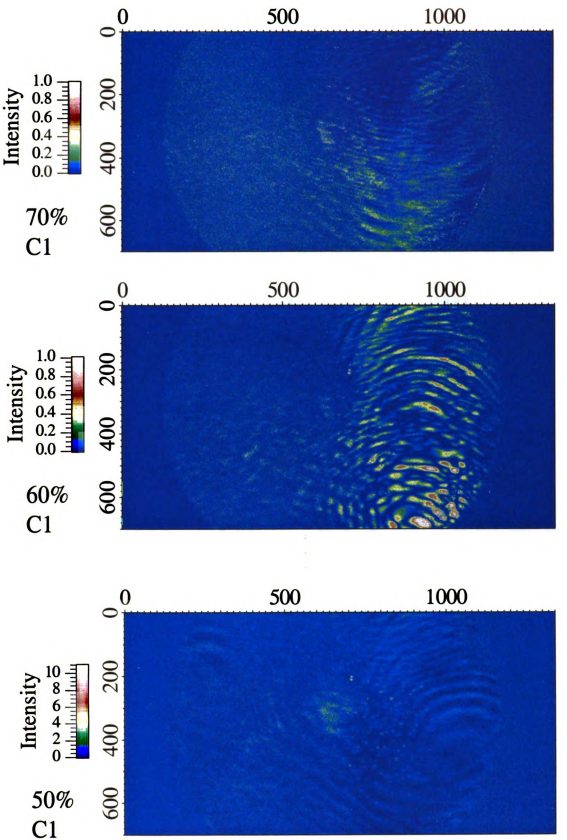
0
500
1000
0
200
400
600
Intensity
1.0
0.8
0.6
0.4
0.2
0.0
70%
C1
60%
C1
10
8
6
4
2
0
50%
C1

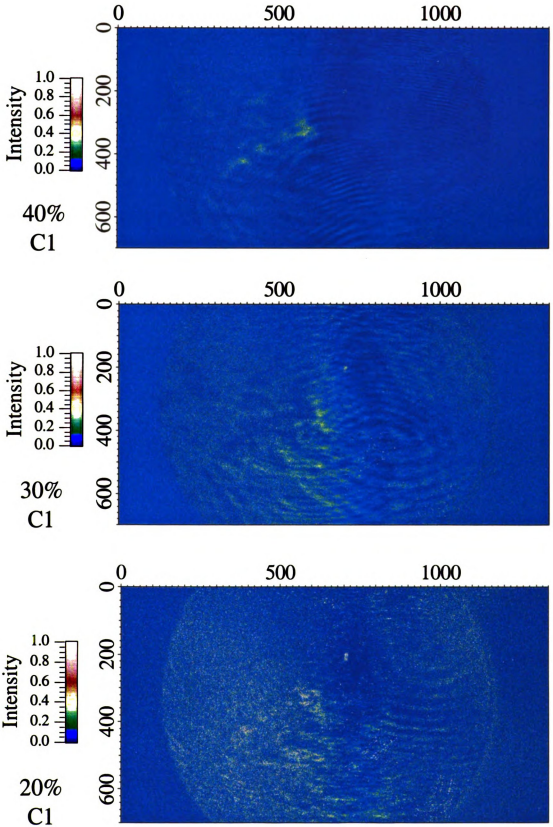
0
500
1000
0
200
400
600
Intensity
1.0
0.8
0.6
0.4
0.2
0.0
40%
C1
30%
C1
20%
C1

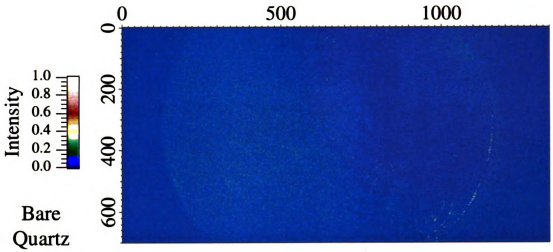
0
500
1000
0
200
400
600
Intensity
1.0
0.8
0.6
0.4
0.2
0.0
Bare
Quartz

APPENDIX B

AUTOCORRELATION FUNCTIONS FOR C1 AND C2 MULTILAYER ASSEMBLIES

This appendix contains all of the AC functions calculated for the C1 and C2 multilayer assemblies. Each autocorrelation function was calculated for a 100 x 100 pixel array taken from the raw image. The C1 assembly exhibits a decrease in correlation with increasing number of layers, however no such trend was observed for the C2 sample.

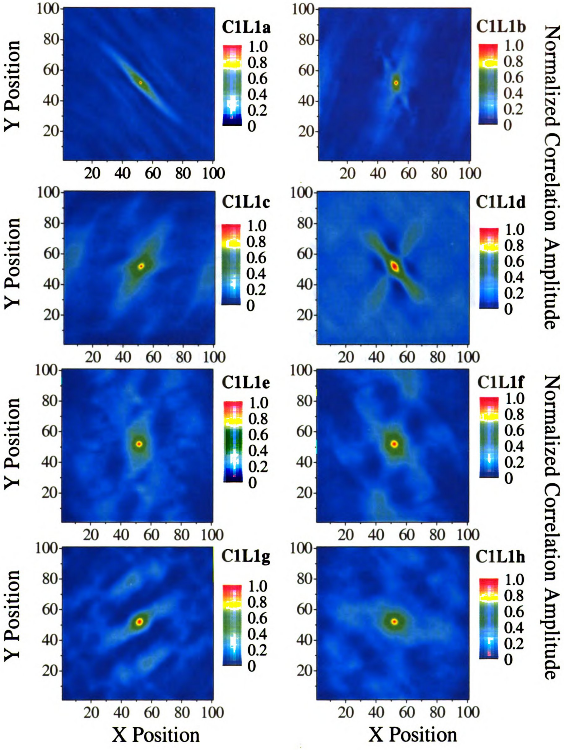
C1L1a
C1L1b
C1L1c
C1L1d
C1L1e
C1L1f
C1L1g
C1L1h
1.0
0.8
0.6
0.4
0.2
0
Y Position
X Position
20
40
60
80
100
Normalized Correlation Amplitude

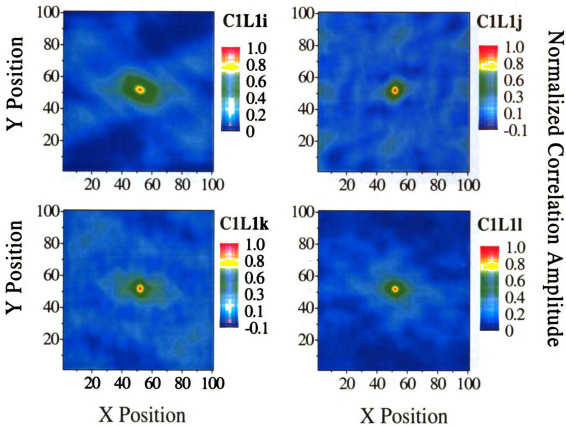
C1L1i
C1L1j
C1L1k
C1L1l
Y Position
X Position
Normalized Correlation Amplitude
1.0
0.8
0.6
0.4
0.3
0.2
0.1
0
-0.1
20 40 60 80 100

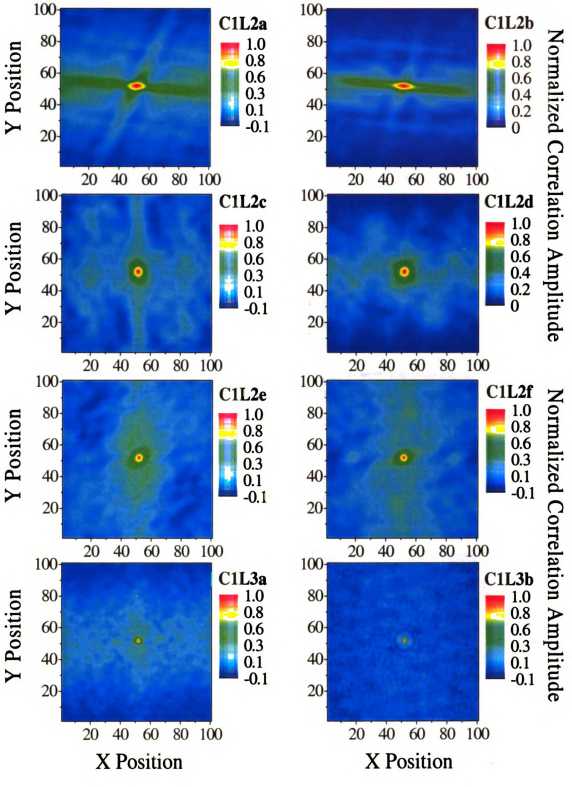
C1L2a
C1L2b
C1L2c
C1L2d
C1L2e
C1L2f
C1L3a
C1L3b
Y Position
X Position
Normalized Correlation Amplitude
1.0
0.8
0.6
0.4
0.3
0.2
0.1
0
-0.1
20
40
60
80
100

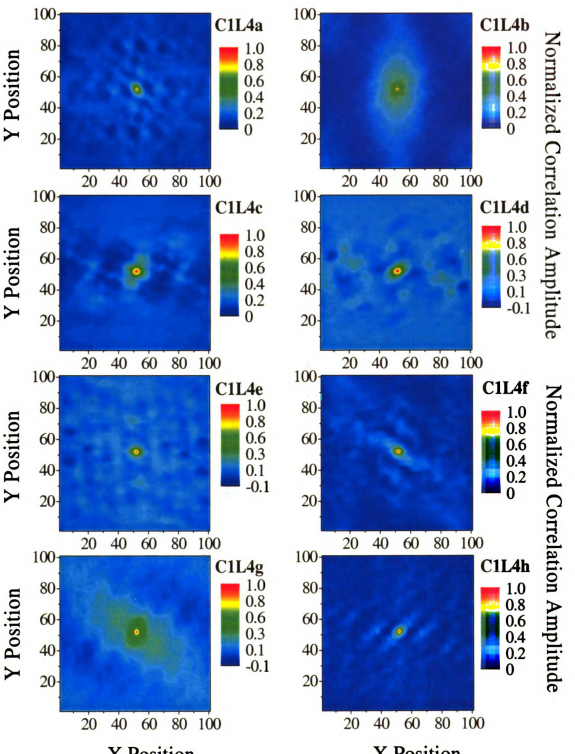
C1L4a
C1L4b
C1L4c
C1L4d
C1L4e
C1L4f
C1L4g
C1L4h
Y Position
X Position
Normalized Correlation Amplitude
1.0
0.8
0.6
0.4
0.3
0.2
0.1
0
-0.1
20
40
60
80
100

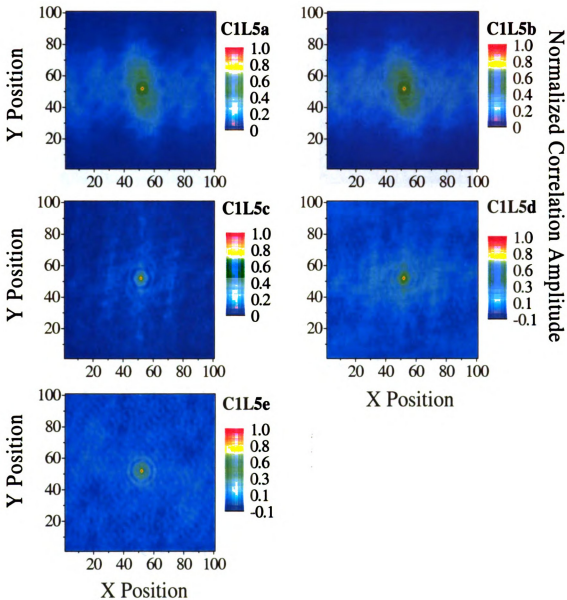
C1L5a
C1L5b
C1L5c
C1L5d
C1L5e
Y Position
X Position
Normalized Correlation Amplitude
1.0
0.8
0.6
0.4
0.3
0.2
0.1
0
-0.1
20 40 60 80 100

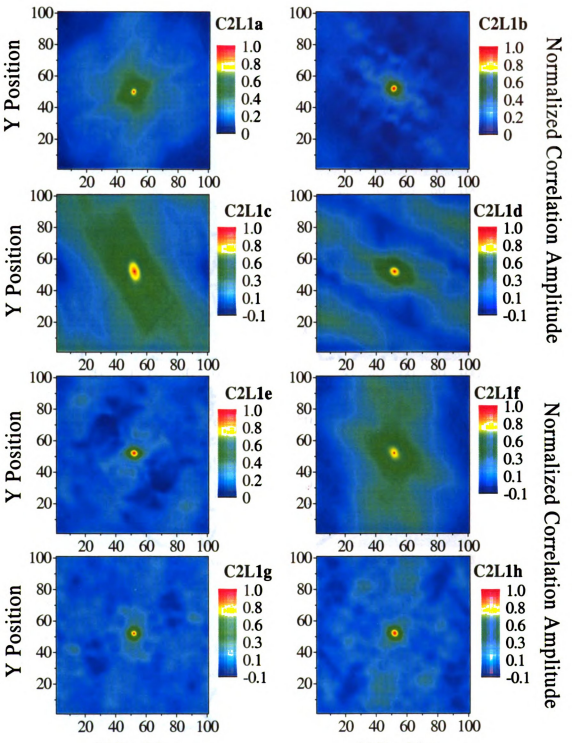
C2L1a
C2L1b
C2L1c
C2L1d
C2L1e
C2L1f
C2L1g
C2L1h
Y Position
X Position
Normalized Correlation Amplitude
Normalized Correlation Amplitude

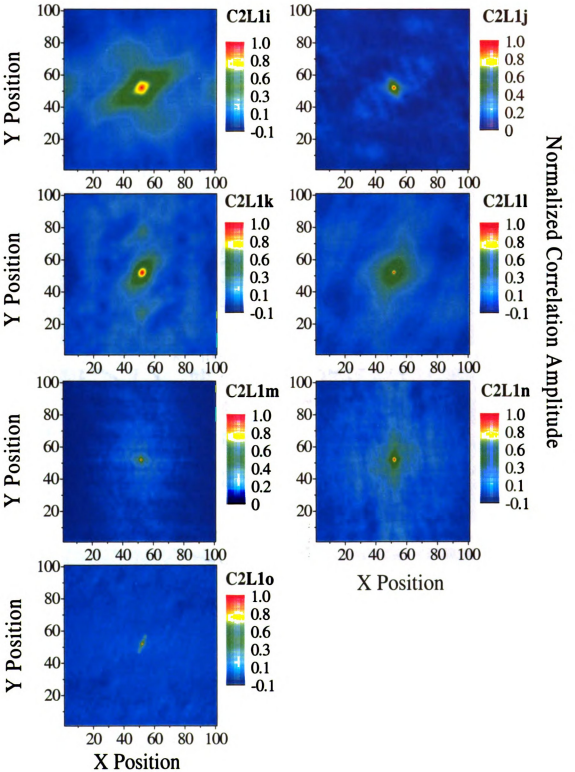
C2L1i
C2L1j
C2L1k
C2L1l
C2L1m
C2L1n
C2L1o
Y Position
X Position
Normalized Correlation Amplitude
1.0
0.8
0.6
0.4
0.3
0.2
0.1
0
-0.1
20
40
60
80
100

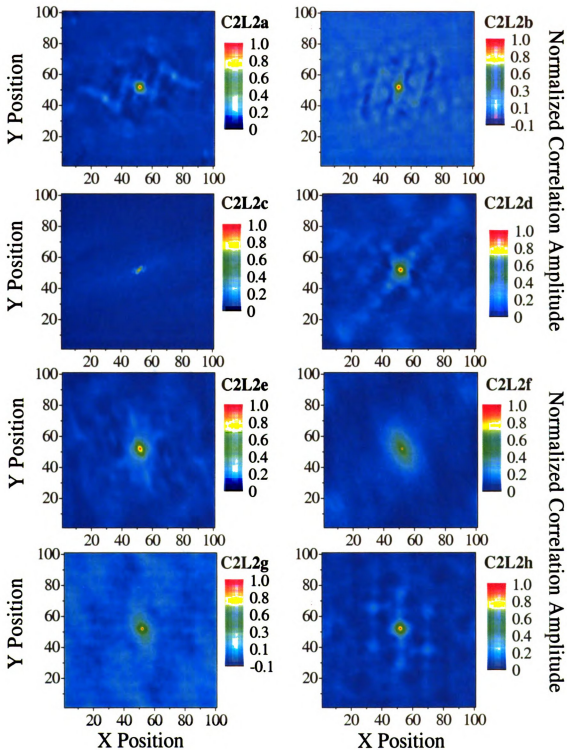
C2L2a
C2L2b
C2L2c
C2L2d
C2L2e
C2L2f
C2L2g
C2L2h
Y Position
X Position
Normalized Correlation Amplitude
1.0
0.8
0.6
0.4
0.3
0.2
0.1
0
-0.1
20
40
60
80
100

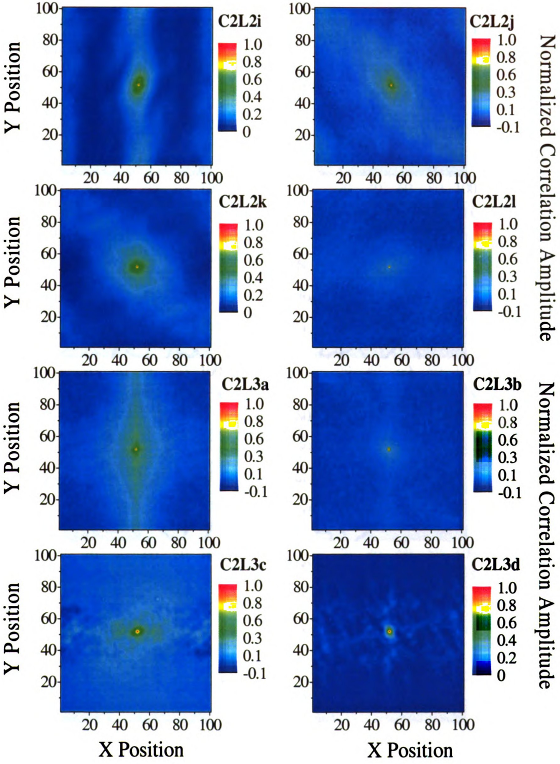
C2L2i
C2L2j
C2L2k
C2L2l
C2L3a
C2L3b
C2L3c
C2L3d
Y Position
X Position
Normalized Correlation Amplitude
1.0
0.8
0.6
0.4
0.3
0.2
0.1
0
-0.1
20
40
60
80
100

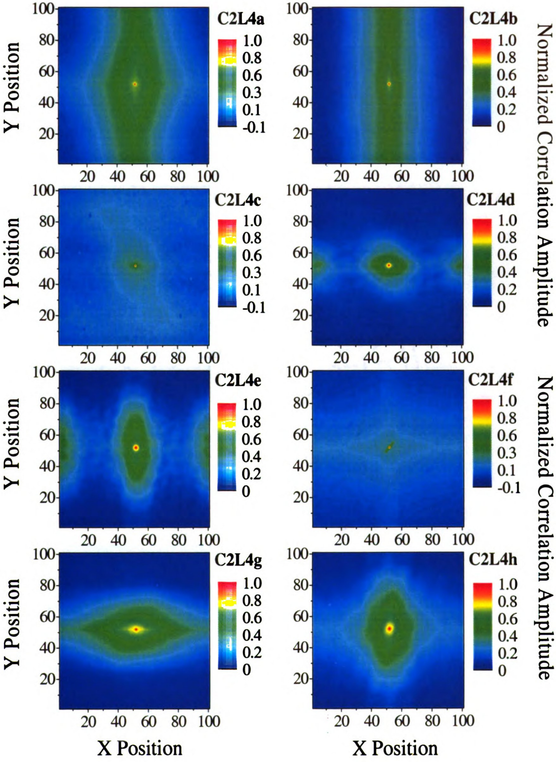
C2L4a
C2L4b
C2L4c
C2L4d
C2L4e
C2L4f
C2L4g
C2L4h
Y Position
X Position
Normalized Correlation Amplitude
1.0
0.8
0.6
0.4
0.3
0.2
0.1
0
-0.1
20
40
60
80
100

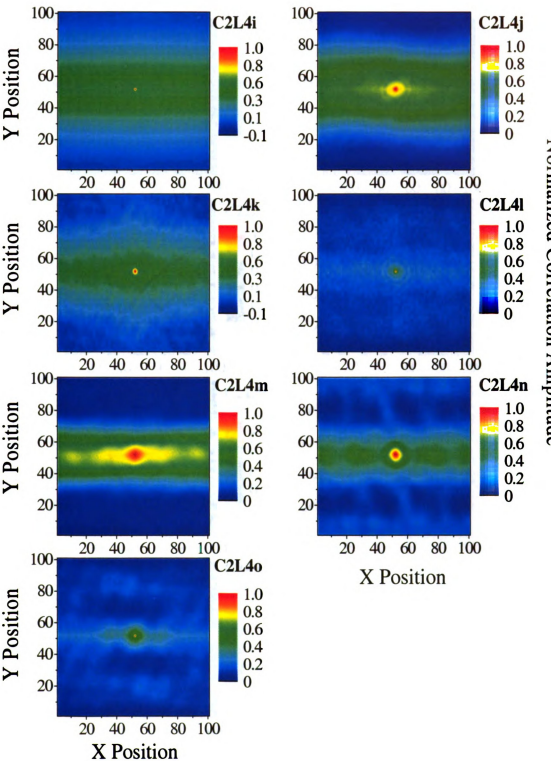
C2L4i
C2L4j
C2L4k
C2L4l
C2L4m
C2L4n
C2L4o
Y Position
X Position
Normalized Correlation Amplitude
1.0
0.8
0.6
0.4
0.3
0.2
0.1
0
-0.1
20
40
60
80
100

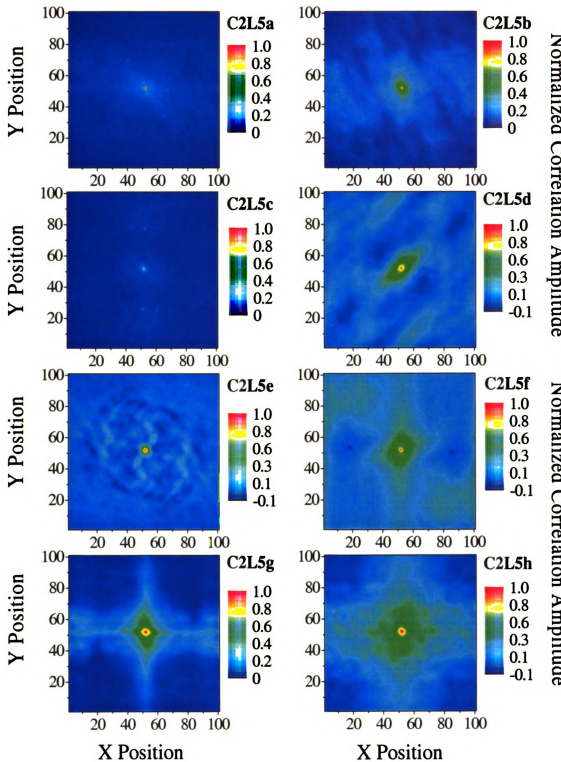
C2L5a
C2L5b
C2L5c
C2L5d
C2L5e
C2L5f
C2L5g
C2L5h
Y Position
X Position
Normalized Correlation Amplitude
100
80
60
40
20
20 40 60 80 100
1.0
0.8
0.6
0.4
0.3
0.2
0.1
0
-0.1